Direct numerical simulation of shock-wave/ boundary layer interaction controlled with convergent–divergent riblets

Tongbiao Guo, Jian Fang, Ji Zhang, and Xinliang Li

Published version information

Citation: T Guo et al. Direct numerical simulation of shock-wave/boundary layer interaction controlled with convergent–divergent riblets. Phys Fluids 34, no. 8 (2022): 086101

DOI: 10.1063/5.0102261

Physics of Fluids

Direct numerical simulation of shock-wave/boundary layer interaction controlled with convergent–divergent riblets

Cite as: Phys. Fluids **34**, 086101 (2022); https://doi.org/10.1063/5.0102261
Submitted: 08 June 2022 • Accepted: 09 July 2022 • Accepted Manuscript Online: 10 July 2022 •
Published Online: 01 August 2022

Tongbiao Guo (郭同彪), **Jian Fang** (方剑), **Ji Zhang** (张吉), **et al.**

Physics of Fluids ARTICLE scitation.org/journal/phf

Direct numerical simulation of shock-wave/boundary layer interaction controlled with convergent–divergent riblets

Cite as: Phys. Fluids **34**, 086101 (2022); doi: 10.1063/5.0102261
Submitted: 8 June 2022 · Accepted: 9 July 2022 ·
Published Online: 1 August 2022

Tongbiao Guo (郭同彪),[1] Jian Fang (方剑),[2] Ji Zhang (张吉),[1,3] and Xinliang Li (李新亮)[1,3,a)]

AFFILIATIONS

[1] LHD, Institute of Mechanics, Chinese Academy of Sciences, Beijing 100190, China
[2] Scientific Computing Department, STFC Daresbury Laboratory, Warrington WA4 4AD, United Kingdom
[3] School of Engineering Science, University of Chinese Academy of Sciences, Beijing 100049, China

[a)] Author to whom correspondence should be addressed: lixl@imech.ac.cn

ABSTRACT

In this paper, a section of convergentdivergent (CD) riblets is applied upstream of a compression ramp in a supersonic turbulent boundary layer in a Mach 2.9 flow with a Reynolds number of $Re_\theta = 2240$. Direct numerical simulations are undertaken to examine the impact of CD riblets on the shock wave/boundary layer interaction and the feasibility of using them to mitigate flow separation. Over the riblet section, a large-scale secondary roll mode is produced by CD riblets with the downwelling motion occurring around the diverging region and upwelling motion near the converging region. This consequently leads to a spanwise heterogeneity in mean quantities and turbulent structures over the riblet section and also in the interaction zone. Compared with the baseline case, the area of the separation zone for the riblet case experiences a dramatic local reduction of 92% in the diverging region, owing to the downwelling motion that injects the high-momentum fluid toward the wall and the near-wall spanwise velocity that transports the low-momentum fluid away. The enhanced upwelling motion around the converging region induced by CD riblets, on the one hand, contributes to the decrease of the near-wall momentum and subsequently the increase of the local separation area. On the other hand, the upwelling motion effectively reduces the incoming Mach number upstream of the compression corner. This appears to reduce the strength of the separation shock, leading to a more gradual compression of the incoming flow that helps ease the enlargement of the separation area nearby. Overall, the area of the mean flow separation is reduced by 56%, indicating an effective flow separation control by the CD riblets.

I. INTRODUCTION

The shock wave/boundary-layer interaction (SWBLI) is a ubiquitous flow phenomenon in supersonic/hypersonic internal and external flows, such as the inlet of the supersonic engine, over-expanded nozzles, control surfaces, and so on. The shock brings a strong adverse pressure gradient that can lead to the flow separation, which results in a degradation of aerodynamic performance such as increased aerodynamic drag, unsteady pressure loads, and even an inlet unstart. It is, therefore, of a great importance to develop effective flow control methods to alleviate the detrimental effects caused by SWBLI.

In the recent decades, a variety of flow control methods has been explored in the SWBLI community such as active control using air-jet vortex generators[1] and plasma energy deposition[2] as well as passive control using bumps[3] and vortex generators.[4,5] Among them, vortex generators have attracted a large volume of research attentions,[4–7] owing to their simplicity in implementation, strong robustness, and control effectiveness. Via promoting the momentum exchange between the near-wall and outer flow, vortex generators are capable of energizing near-wall fluid, and increasing its ability of resisting adverse pressure gradient. Despite their ability in suppressing flow separation, conventional vortex generators bring large parasitic drag due to their macro-scale size which compromises their flow control benefit. As a result, more research attentions have been shifted to the studies of the micro-vortex generators (or low-profile vortex generators)[5] which have a typical height of $0.2\delta_0$–$0.7\delta_0$ (δ_0 is the boundary layer thickness). Nevertheless, with the increase of Mach number, the micro-vortex generators begin to be exposed to the high-speed field and bring a considerable amount of parasitic drag. Although a further decrease of the device height can reduce the parasitic drag, the micro-vortex generators would become ineffective[5,8] with a height less than

$0.1\delta_0$–$0.3\delta_0$. Rybalko *et al.*[8] reported that no control effect was obtained when the device height was decreased to $0.35\delta_0$ in the external compression low-boom inlets. As such, other passive flow control techniques that are capable of mitigating the flow separation with less parasitic drag are still being sought.

Convergentdivergent (CD) riblets are inspired by the surface structures on the sharks' skin[9] and on the secondary flight feathers of birds.[10] Owing to their potential in performing the flow separation control,[11–13] CD riblets have received a large amount of research attentions in recent years.[10,14–17] As depicted in Fig. 1, CD riblets are usually composed of left-tilted and right-tilted micro-groove sections arranged in an alternative manner in the spanwise direction. From the view of the incoming flow, the streamwise line along which microgrooves on adjacent riblet sections appear to diverge away from is called the diverging line (DL), whereas the line on which microgrooves on adjacent riblet sections appear to converge toward each other is called the converging line (CL). The riblet height h is usually less than $0.05\delta_0$ with $h^+ < 20$ (the superscript, $+$, stands for a quantity scaled with the local wall units)[10,14–17] in turbulent flows.

Koeltzsch *et al.*[9] conducted experimental studies in a turbulent pipe with the inner surface fitted with CD riblets. They found that in comparison to the baseline case with the smooth wall, CD riblets led to an increased streamwise velocity and decreased turbulent fluctuations around the DL, and an opposite trend occurred near the CL. In a flat-plate turbulent boundary layer flow developing over CD riblets, Nugroho *et al.*[14] revealed a time-averaged large-scale secondary roll mode for the first time using hot-wire measurements in the wall-normal-spanwise plane over each riblet section. The induced roll mode produced the downward/upward motions around the DL/CL and consequently led to an apparent spanwise variation of the streamwise velocity and the turbulent intensity. This occurrence of the large-scale roll mode has also been confirmed by Kevin *et al.*[15] and Xu *et al.*[18] in a turbulent boundary layer based on the stereoscopic particle image velocimetry technique and by Benschop and Breugem[19] and Guo *et al.*,[17] who performed a series of direct numerical simulations (DNSs) in a fully developed turbulent channel flow with CD riblets mounted on the wall.

The fact that CD riblets are capable of generating a large-scale secondary flow motion that enhances the momentum transfer across the boundary layer indicates the potential of the CD riblets in mitigating the flow separation in some ways similar with the vortex generators. Quan *et al.*[11] applied an array of CD riblets upstream of a double ramp and found that CD riblets were capable of mitigating the shock-induced flow separation in supersonic laminar flows. Liu *et al.*[12] placed an array of CD riblets over the suction surface of diffuser blades in a linear cascade, and the experimental results revealed a reduction of 36.4% in the zone-averaged pressure loss coefficient. However, the boundary layer in both experiments was so thin (less than 1 mm) that the near-wall flow field within the boundary layer could not be obtained due to the limitation of experimental measurement, to enable a detailed examination of the interaction between CD riblets and the separating boundary layer. Consequently, the mechanism underlying the flow separation control remains unclear. It is worth mentioning that the existed study on the large-scale secondary flow induced by CD riblets has been all conducted in incompressible flows, and no investigation has been made in a supersonic flow where the separation is induced by a shock wave. These issues provide the motivation for undertaking the present work.

In this paper, the control effect of CD riblets in a supersonic SWBLI at a Mach number of 2.9 is studied via a direct numerical simulation (DNS) approach. CD riblets are applied in the flat-plate turbulent boundary layer upstream of a 24° compression ramp, as seen in Fig. 1(a). The influence of CD riblets on the flow field upstream of and around the SWBLI zone is examined, and the control mechanism in mitigating the shock-induced flow separation is explored, aiming to provide an insight to the flow separation control mechanism by CD riblets in compressible flow. To our best knowledge, this is the first study of exploring the use of CD riblets for the shock-induced flow separation in a shock wave/turbulent boundary-layer interaction caused by the compression ramp. This paper is organized as follows. In Sec. II, the geometry of the CD riblets and the numerical methods are described. Section III presents the results and discussions before some conclusions are drawn in Sec. IV. Finally, a grid-sensitive study is performed to ensure sufficient mesh resolution for the flow field analysis in the Appendix.

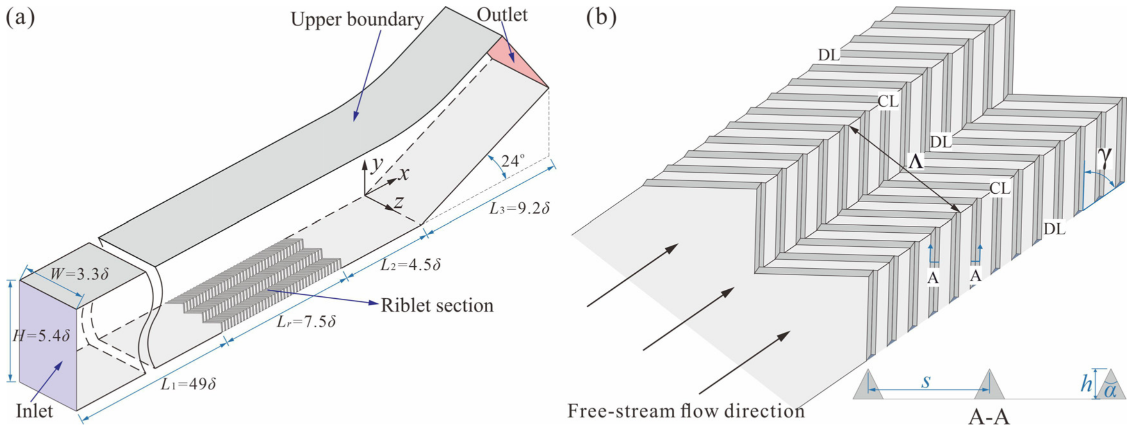

FIG. 1. (a) Sketch of the computational domain. (b) Schematic diagram of CD riblets with definitions of the diverging line (DL), converging line (CL), riblet spacing (s), riblet height (h), ridge angle (α), riblet wavelength (Λ), and yaw angle (γ). δ is the boundary layer thickness at the starting position of the riblet section ($x = -12\delta$).

TABLE I. Properties of the incoming flow and the turbulent boundary layer at $x/\delta = -12$.

Case	Ma_∞	T_∞ (K)	T_w (K)	δ (mm)	θ (mm)	Re_θ	C_f
Bookey *et al.*[26]	2.9	107.1	307	6.7	0.43	2400	0.002 25
Wu and Martin[27]	2.9	108.1	307	6.4	0.38	2300	0.002 17
Present DNS	2.9	108.1	307	6.6	0.40	2240	0.002 31

II. METHODOLOGY

A. Computational domain and C–D riblets geometry

The present studies are undertaken in a supersonic turbulent boundary layer with a 24° turning angle of the compression ramp, as seen in Fig. 1(a). The coordinate system adopted in the present study is also shown with its origin located at the compression corner. The streamwise, vertical and spanwise directions are denoted by x, y, and z, respectively, and the corresponding velocity components are u, v, and w. The computational domain size is the same for all the cases with the streamwise length $L = 61\delta$, the height $H = 5.4\delta$, and the spanwise width $W = 3.3\delta$, where δ is the boundary layer thickness at $x = -12\delta$ in the baseline case without CD riblets, and δ is used as the reference length in this study. For the case with CD riblets, $L = L_1 + L_r + L_2 + L_3$ [Fig. 1(a)], where $L_r = 7.5\delta$ is the streamwise length of the riblet section that begins from $x = -12\delta$ to -4.5δ; L_1 and L_2 denote the streamwise length before and after the riblet section in the flat plate; L_3 represents the streamwise length of the ramp.

The CD riblet parameters are shown in Fig. 1(b). The acute angle that the riblet passage forms with DL is called the yaw angle γ with $\gamma = 45°$. The spanwise width of two adjacent DL or CL is the wavelength Λ with $\Lambda = 1.1\delta$, and in the present study, there are three riblet wavelengths in the spanwise direction. The setting of γ and Λ has been found to produce a strong large-scale secondary flow motion[17,20] when the other riblet parameters are fixed. Riblets with trapezoidal cross sections are used with the riblet height, spacing and ridge angle being $h = \delta/30$, $s = 4h$, and $\alpha = 80°$, respectively.

B. Governing equations and numerical schemes

An in-house high-order finite-difference computational fluid dynamics code (OPENCFD-SC)[21] is adopted as the solver of the present study. This code has been used successfully in many supersonic shock wave/turbulent boundary-layer interaction studies.[21–24] In this code, the unsteady, three-dimensional, compressible NavierStokes (N–S) equations in a curvilinear coordinate system (ξ, η, ζ) expressed below are solved,

$$\frac{\partial Q}{\partial t} + \frac{\partial (F - F_v)}{\partial \xi} + \frac{\partial (G - G_v)}{\partial \eta} + \frac{\partial (H - H_v)}{\partial \zeta} = 0, \qquad (1)$$

where t is the time coordinate; Q represents the conservative variables; F, G, and H are the convective flux terms in the ξ, η, and ζ directions, respectively; F_v, G_v, and H_v are the corresponding diffusion terms with the viscosity coefficient calculated via Sutherland's law. The N–S equations are non-dimensionalized with the unit reference length and free-stream incoming quantities, including the velocity U_∞, the temperature T_∞, and the density ρ_∞. The perfect gas state equation is enforced to close the NS equations with a gas constant of $R = 287.1$ J/(kg K).

The convective terms are discretized by a hybrid difference scheme which adapts its form according to the shock sensor introduced by Jameson *et al.*[25] The seventh-order upwind linear scheme is applied in smooth parts of the flow field to maximize the resolving efficiency, while around the shock wave a seventh-order WENO (weighted essentially-non-oscillatory) scheme is used to improve numerical stability. The diffusion terms are discretized with an eighth-order central difference scheme. After all the spatial terms are solved, the three-step third-order Runge–Kutta method is applied for the temporal integration.

C. Computational setting and mesh

Two cases of DNSs are conducted in the present study, i.e., the baseline case without the CD riblets and the controlled case with the CD riblets. The free-stream conditions are similar to those in the experiments of Bookey *et al.*[26] and the DNS of Wu and Martin,[27] as seen in Table I. The free-stream Mach number Ma_∞ is 2.9, and the free-stream temperature T_∞ is 108.1 K. The Reynolds number for the baseline case based on the momentum thickness θ of the turbulent boundary layer at $x/\delta = -12$ is $Re_\theta = 2240$. The corresponding friction Reynolds number $Re_\tau = U_\tau \delta / \bar{\nu}_w$ (U_τ is the mean friction velocity; $\bar{\nu}_w$ is the mean fluid kinematic viscosity at the wall) is 306. The riblets' height and spacing scaled with the wall units of the baseline case are $h^+ = hU_\tau/\bar{\nu}_w = 10.2$ and $s^+ = sU_\tau/\bar{\nu}_w = 40.8$. The non-dimensional time step $\Delta t U_\infty/\delta$ for the baseline case is 0.0015, while for the riblet case, the time step reduces to $\Delta t U_\infty/\delta = 0.0005$.

On the bottom wall, the isothermal no-slip boundary condition is enforced with constant wall temperature $T_w/T_\infty = 2.84$. At the inlet, a steady laminar boundary layer profile is enforced, which is obtained from the auxiliary simulation of a laminar flat-plate boundary layer using the same free-stream conditions and wall temperature. To trigger the transition to turbulence, the periodic wall blowing and suction[28] is applied in the region ranging from $x/\delta = -58$ to $x/\delta = -55$ (see Fig. 2). The nonreflecting boundary condition is enforced

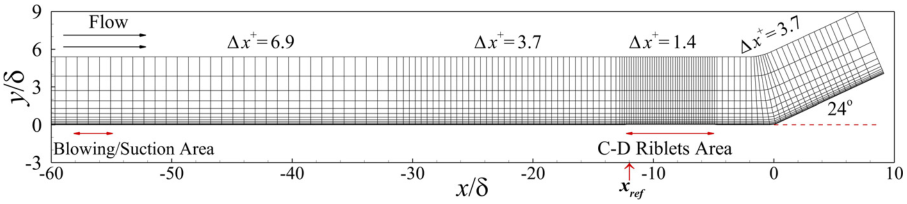

FIG. 2. Mesh distribution in the x–y plane for the CD riblet case. The mesh is plotted every 40th and 20th grid line in the x and y directions for the convenience of visualization.

TABLE II. Computational domain size and mesh distributions for DNS cases. The superscript + denotes variables in wall units, calculated based on the wall friction velocity of the baseline case at $x/\delta = -12$.

Case	Re_θ	L/δ	H/δ	W/δ	N_x	N_y	N_z	Δx^+	Δy^+	Δz^+
Baseline	2240	61	5.4	3.3	4591	240	336	6.9, 3.7, 1.4, 3.7	0.45 ~	3.0
Riblet	2240	61	5.4	3.3	5640	240	336	6.9, 3.7, 3.7, 3.7	0.25 ~	3.0

on the top boundary, and the periodic boundary condition is applied in the spanwise direction. To eliminate the disturbance reflection at the outlet, a buffer region with progressively coarsening mesh distribution is applied near the outlet (see Fig. 2), and the second-order zero-gradient extrapolation boundary condition is applied at the outlet plane.

The structured mesh is used to discretize the computational domain, and the number of grid points in each direction is shown in Table II. The mesh distribution in the longitudinal ($x-y$) plane is shown in Fig. 2, where the grid line is plotted every 40th and 20th grid line in the x and y directions for the convenience of visualization. The grid size in the streamwise direction is also shown where the superscript "+" denotes variables in wall units, calculated based on the wall friction velocity of the baseline case at $x/\delta = -12$. In the vertical direction, a non-uniform mesh based on a geometric progression with a constant ratio was applied, and the first grid point away from the wall is $y^+ = 0.25$ at the riblet tip and located within $0.25 \le y^+ \le 0.45$ at other places. The mesh topology in the vicinity of the streamwise starting position of the riblet section is shown in Fig. 3(a), where the mesh is plotted every fourth, eighth, and eighth grid line in the x, y, and z directions, respectively. In the spanwise direction, a uniform mesh is used with $\Delta z^+ = 3.0$. The mesh distribution near the ribbed wall in the x–y plane is further displayed in Fig. 3(b), and it can be seen that the mesh is nearly orthogonal in the vicinity of the riblets.

D. Validation using the baseline case without C–D riblets

To validate the present DNS, the results of the baseline case without riblets are compared with the existed DNS and experimental data. Figure 4(a) shows the contour of the instantaneous numerical schlieren $DS = 0.8\exp[-10(|\nabla\rho| - |\nabla\rho|_{\min})/(|\nabla\rho|_{\max} - |\nabla\rho|_{\min})]|\nabla\rho|$. The definition of DS is suggested by Wu and Martin[27] to enhance the small-density gradient in the flow field. Regions of high-density

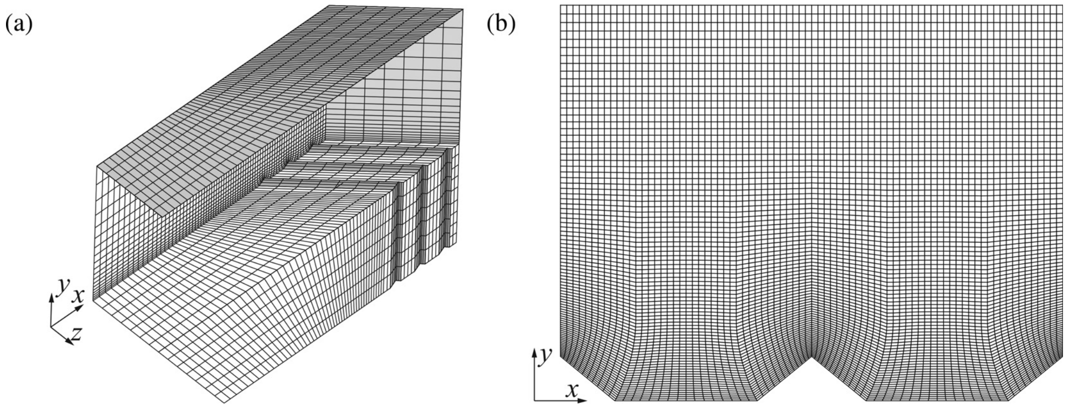

FIG. 3. (a) Illustration of the computational meshes near the starting position of riblet section with the mesh plotted every fourth, eighth, and eighth grid line in the x, y, and z directions, respectively. (b) Mesh distribution in the vicinity of the ribbed wall in the x–y plane.

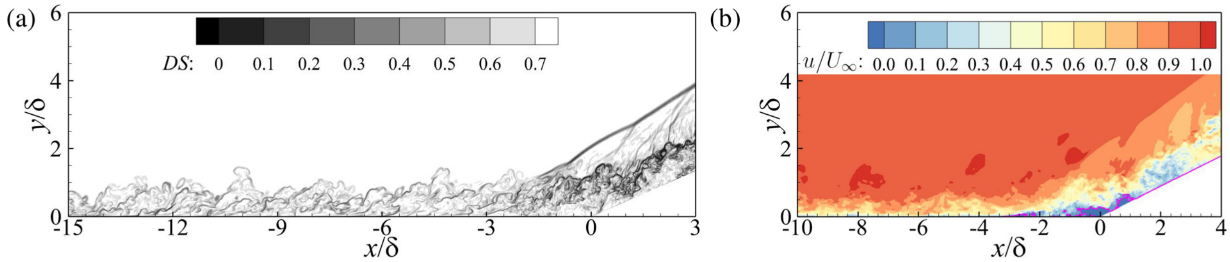

FIG. 4. Contours of the instantaneous (a) numerical schlieren and (b) streamwise velocity in the x-y plane.

gradient in this figure are denoted with the dark gray color. The main shock is clearly observed with its shock foot penetrated into the boundary layer. A few shocklets emanate from the near wall region downstream of the compression corner, and then, they merge into the main shock. The instantaneous flow characteristics are the same with the DNS result of Wu and Martin.[27] Figure 4(b) shows the contour of the instantaneous streamwise velocity, where the pink line denotes the locus of the zero-streamwise velocity. It can be seen that the reversed flow occurs around the corner region as a result of the interaction with the shock wave.

In the following analysis, the Reynolds and density-weighted averaging operations are incorporated, which are, respectively, defined as, $\bar{\phi} = (1/T)\int_T \phi dt$ and $\langle\phi\rangle = \overline{\rho\phi}/\bar{\rho}$, for a general variable ϕ. The fluctuations from the Reynolds and density-weighted averaging operations can be, therefore, expressed as, $\phi' = \phi - \bar{\phi}$ and $\phi'' = \phi - \langle\phi\rangle$. Figure 5 shows the profiles of the mean van Driest transformed streamwise velocity and Reynolds stress from the baseline case at $x/\delta = -12$. It can be seen that the mean velocity profile obtained from our simulation agrees well with the classic law of wall for a turbulent boundary layer, indicating that the flow at the station has fully developed to a turbulent state. The DNS results of Wu and Moin[29] and Spalart[30] are also included in Fig. 5 for comparison. One can see that the present results match very well with the previous DNS results, verifying that the present DNS in the undisturbed supersonic turbulent boundary layer is credible.

The wavenumber spectra of the streamwise velocity fluctuations (E_{uu}), vertical fluctuations (E_{vv}), spanwise fluctuations (E_{ww}), and turbulence kinetic energy (E_k) in the spanwise direction at $(x, y) = (-12\delta, 0.2\delta)$ are presented in Fig. 6. One can see that the spectra have gone through the $-5/3$ slop for all the components although the $-5/3$ region is relatively short due to the low Reynolds number in the present study. At the high wavenumbers, the spectra drop due to the dissipation at small scales, and there is no evidence of energy pileup, indicating that the grid resolution and the spanwise direction are adequate,[31] and the numerical method is properly implemented.

Figure 7 shows the mean skin friction coefficient $C_f = \bar{\tau}_w/(0.5\rho_\infty U_\infty^2)$ ($\bar{\tau}_w$ denotes the mean wall shear stress) and the mean wall pressure $\bar{p}_w$ in the vicinity of the compression ramp. One can see that both C_f and $\bar{p}_w$ agree well with the experimental results of Bookey *et al.*[26] and the DNS data of Wu and Martin,[27] whose flow configuration and free-stream conditions are very close to the present baseline case (see Table I). The locations of the separation and reattachment points, defined as the zero-C_f points, also match the results from Bookey *et al.*[26] and Wu and Martin.[27]

III. RESULTS AND DISCUSSION

In this section, the influence of CD riblets on the flow field in the *y*–*z* and *x*–*y* planes is examined first, and then, the turbulent structures are analyzed.

A. The mean flow field in the *y*–*z* plane

Figure 8 shows contours of the streamwise velocity at a number of *y*–*z* planes in the riblet case, and the results for the baseline case are also included as narrow columns for comparison. One can clearly see that a pair of the secondary roller represented by the mean in-plane streamlines is developed over the riblet section, and a spanwise variation of the mean streamwise velocity is induced due to the large-scale rollers. Along the streamwise direction, the extent of the roll motion appears to increase, and the center of the roll mode tends to move away from the ribbed wall gradually and toward the mid portion between the DL and CL. The contours of the streamwise velocity at $x/\delta = -10.5$ and $x/\delta = -6$ along with the in-plane velocity vectors are presented in Fig. 9, and the results of the baseline case are also provided for comparison. It is clearly seen that the roll mode at $x/\delta = -10.5$ [Fig. 9(a)] is confined within $y/\delta < 0.2$ and the center of the roll motion (denoted by the solid dot symbol) lies at approximately $(y, z) = (0.06\delta, 0.16\Lambda)$. In contrast, at $x/\delta = -6$, the roll mode is extended to 40% of the boundary layer thickness in the vertical direction with its center located at $(y, z) = (0.13\delta, 0.25\Lambda)$, leading to a larger spanwise variation of the streamwise velocity. Such a large-scale roll mode has also been observed in the incompressible turbulent

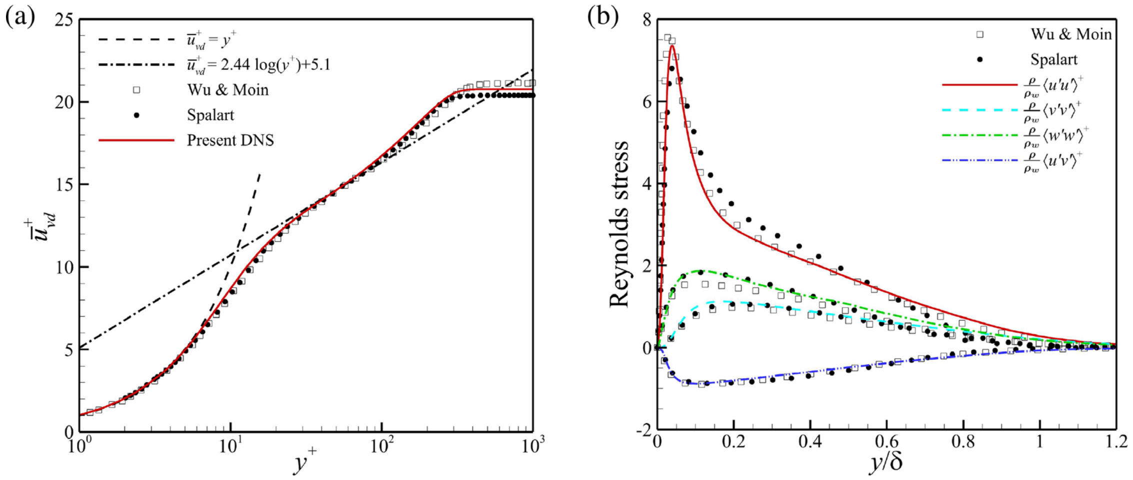

FIG. 5. Profiles of (a) the mean van Driest transformed streamwise velocity and (b) the density-scaled Reynolds stress profiles. The results are taken in the baseline case without riblets at $x/\delta = -12$. $y^+ = yU_\tau/\bar{\nu}_w$; $\bar{u}_{vd}^+ = \frac{1}{U_\tau}\int_0^{\bar{u}} \sqrt{\bar{\rho}/\bar{\rho}_w}\,d\bar{u}$ ($\bar{\rho}_w$ is the mean fluid density at the wall); $\langle u_i'u_j'\rangle^+ = \langle u_i'u_j'\rangle/U_\tau^2$.

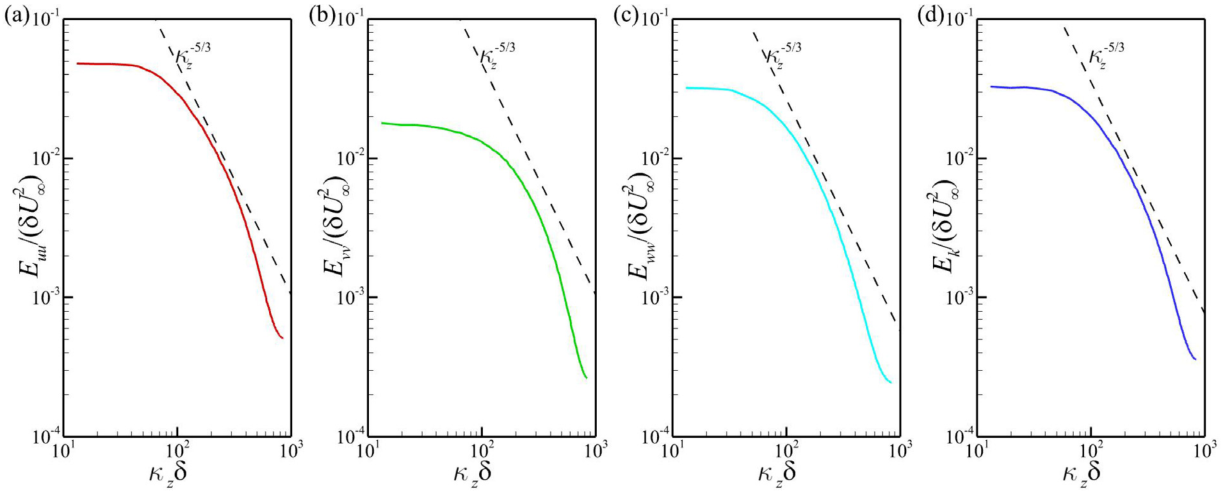

FIG. 6. Wavenumber spectra of the (a) streamwise velocity fluctuations (E_{uu}), (b) vertical fluctuations (E_{vv}), (c) spanwise fluctuations (E_{ww}), and (d) turbulence kinetic energy (E_k) in the spanwise direction at $(x, y) = (-12\delta, 0.2\delta)$. κ_z is the wavenumber in the spanwise direction.

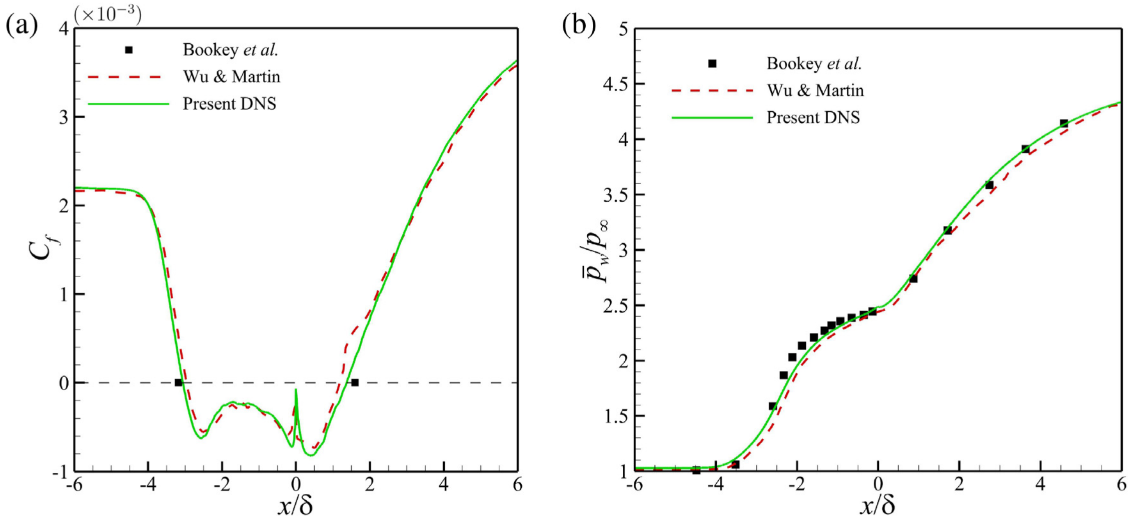

FIG. 7. The streamwise distribution of the mean (a) skin friction coefficient C_f and (b) wall pressure $\bar{p}_w$ in the vicinity of the compression ramp corner for the baseline case.

boundary layer flow[15,18] over CD riblets. The pink line in Fig. 9 denotes the sonic line, and one can see that the riblets are well immersed into the subsonic portion of the boundary layer which may help ease the parasitic drag caused by the riblets.

With a closer examination of the in-plane velocity vectors at $x/\delta = -10.5$ and $x/\delta = -6$ in Fig. 9, it can be seen that, in the riblet case, a large-scale roll mode is generated, which displays downwelling/upwelling motions over the DL/CL and a spanwise motion directing from the DL to the CL closely above the ribbed wall. It has been proved that the near-wall spanwise flow induced by the yawed riblet grooves serves as the driving force of the secondary roll mode.[20,32] The upward motion takes the low-momentum fluid away from the wall, contributing to the decrease of the local streamwise velocity. In contrast, the downward motion transports the high-speed fluid toward the wall and leads to the increased streamwise velocity nearby. It is worthwhile mentioning here that although the roll motion in the y–z plane is clear, its strength is relatively weak, with an in-plane velocity magnitude (denoted by $\sqrt{\bar{v}^2 + \bar{w}^2}$) being less than 3%$U_\infty$ in this case. Due to the geometric symmetry, there exists a pair of counter-rotating recirculating motions over a full riblet wavelength. In the following analysis, results covering only half of a spanwise wavelength are presented for brevity.

At the downstream locations of the riblet section, the difference in the streamwise velocity between the diverging and the converging region (see Fig. 8) is still clearly observed until at least $x/\delta = 3$. The occurrence of the compression ramp leads an apparent upward motion nearby, as seen in Figs. 10(b) and 10(d). As a result, the large-scale roll mode in the riblet case is no longer discernible from the

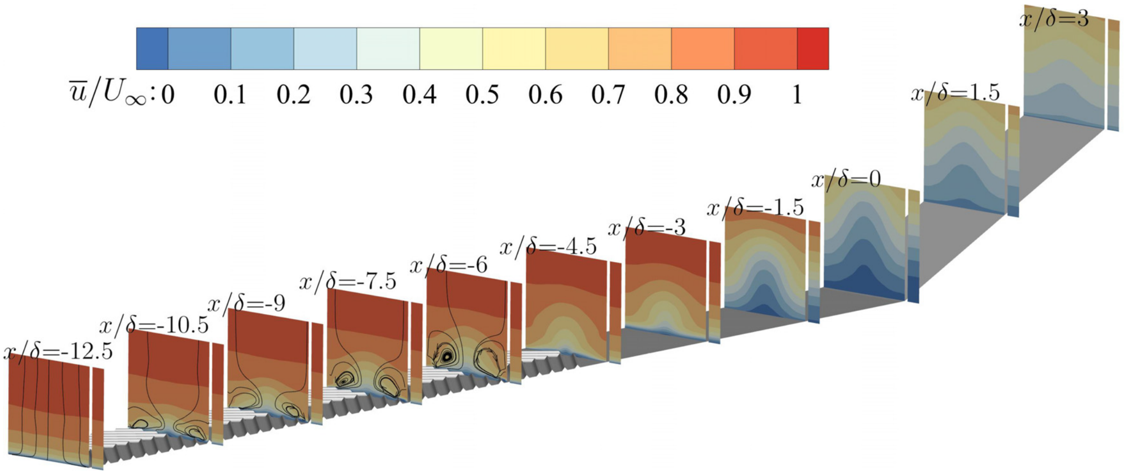

FIG. 8. Contours of the streamwise velocity at a number of *y*–*z* planes in the riblet case. The results for the baseline case are included as narrow columns for comparison.

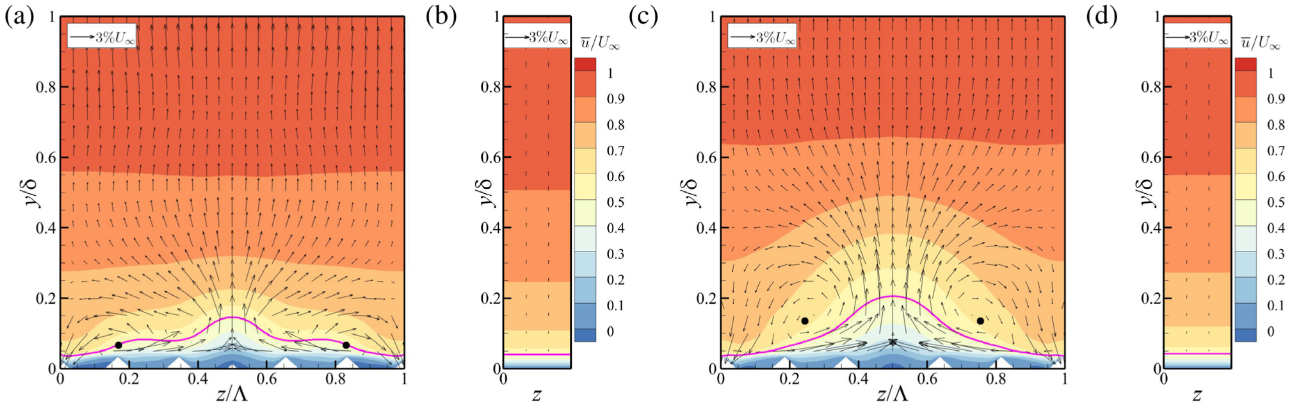

FIG. 9. Contours of the streamwise velocity superimposed with the in-plane velocity vectors in the *y*-*z* plane at [(a) and (b)] $x/\delta = -10.5$ and [(c) and (d)] $x/\delta = -6$ for [(a) and (c)] the riblet case and [(b) and (d)] the baseline case. The solid dot symbol indicates the center of the roll motion. The pink line denotes the sonic line.

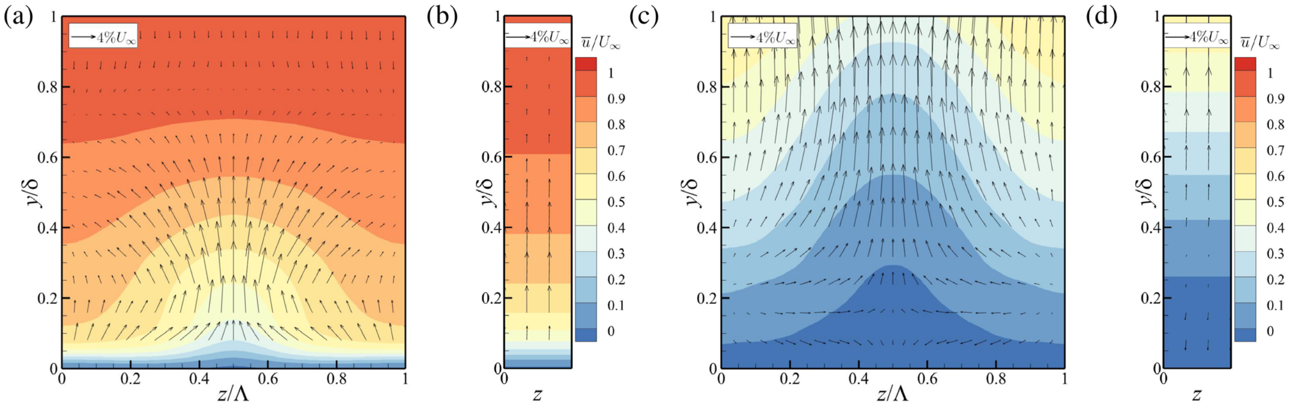

FIG. 10. Contours of the mean streamwise velocity superimposed with in-plane vectors in the *y*-*z* plane at [(a) and (b)] $x/\delta = -3$ (over the riblet section) and [(c) and (d)] $x/\delta = 0$ (compression corner) for [(a) and (c)] the riblet case and [(b) and (d)] the baseline case.

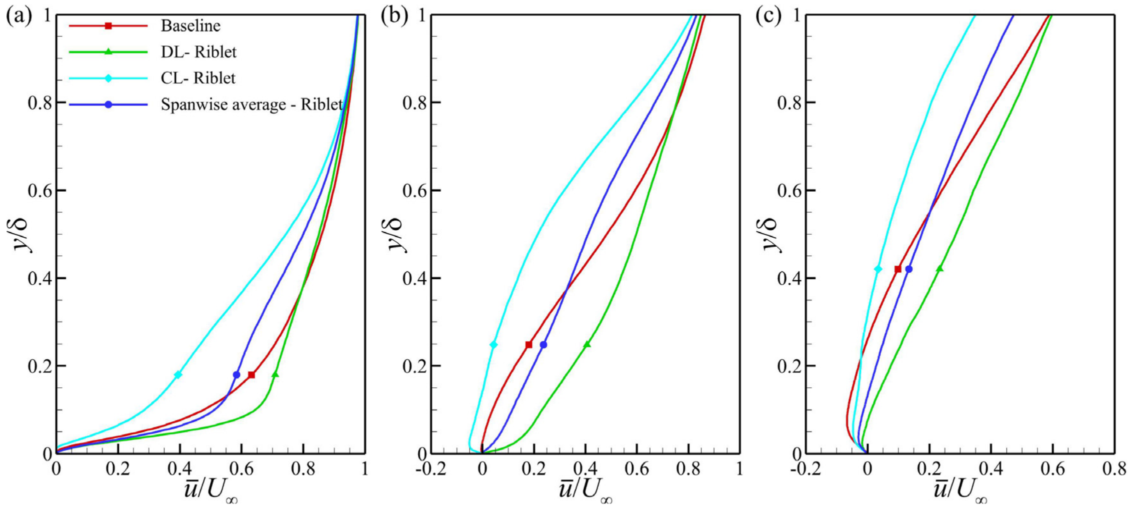

FIG. 11. Profiles of the streamwise velocity for the riblet case over the DL/CL along with the spanwise-average and that in the baseline case at (a) $x/\delta = -3$, (b) $x/\delta = -1.5$, and (c) $x/\delta = 0$.

mean flow field. Nevertheless, the large-scale secondary motion is still clearly revealed by the spanwise flow directing from the DL to the CL, contributing to an apparent spanwise variation of the streamwise velocity. To aid a quantitative comparison, Fig. 11 presents profiles of the mean streamwise velocity for the riblet case over the DL/CL and the spanwise-averaged result at $x/\delta = -3$, $x/\delta = -1.5$, and $x/\delta = 0$. Compared with the baseline case, the streamwise velocity profile over the DL becomes fuller, and the opposite phenomenon occurs over the CL.

Figure 12 presents contours of the mean vertical velocity, fluid density, and temperature in the y-z plane at $x/\delta = -3$. Compared with the baseline case, the vertical velocity around the diverging region is decreased while it is increased significantly near the converging region, which can also be seen by the corresponding profiles over the DL/CL in Fig. 13(a). The redistribution of the vertical velocity leads to an apparent spanwise variation of the density and temperature. In comparison, the fluid density around the DL appears to increase and the temperature is reduced, while the opposite occurs near the CL [see Figs. 12(b), 12(c), 13(b), and 13(c)]. This results from the increased intensity of the upwelling motion around the CL that takes more fluid with low density (high temperature) away from the ribbed wall with the opposite phenomenon occurring around the DL.

B. The mean flow field in the *x-y* plane

1. *Flow separation*

Figure 14 presents contours of the mean streamwise velocity in the *x-y* plane around the compression ramp in the riblet and baseline cases. The pink lines depict the locus of the zero-streamwise velocity with its starting and end points denoting the location of the flow separation and reattachment, and the mean flow separation occurs in the region below the pink lines. Compared with the baseline case, the area of the low-speed zone over the DL is much smaller [Fig. 14(a)], and the reversed flow region almost completely disappears. Along the spanwise direction from the DL to the CL, the region with low-speed fluid and reversed flow tends to increase gradually, peaking over the CL.

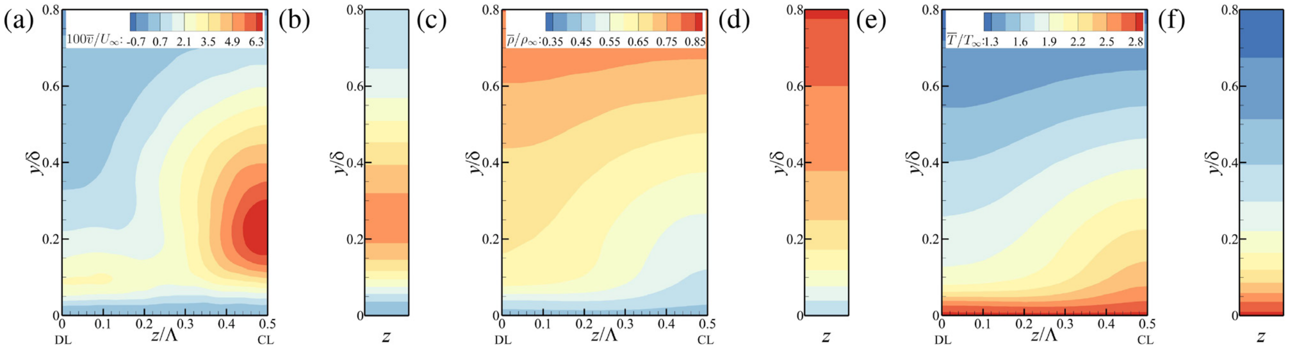

FIG. 12. Contours of the mean [(a) and (b)] vertical velocity, [(c) and (d)] fluid density, and [(e) and (f)] temperature in the *y-z* plane at $x/\delta = -3$ for [(a), (c), and (e)] the riblet case and [(b), (d), and (f)] the baseline case.

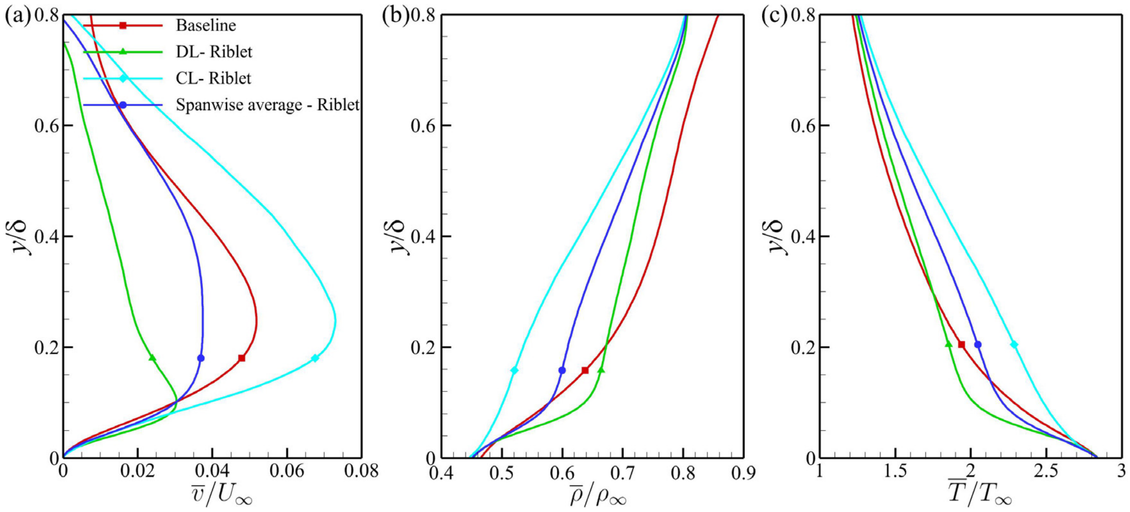

FIG. 13. Profiles of the mean (a) vertical velocity, (b) fluid density, and (c) temperature in the riblet case over the DL/CL and that in the baseline case at $x/\delta = -3$.

With a closer examination of the streamline patterns in Fig. 14, one can see that the separated flow in the baseline case is developed into a closed re-circulation bubble. In contrast, no closed bubble occurs in the riblet case. This is because that the flow separation in the riblet case is three-dimensional, in which the spanwise velocity enables the fluid to escape laterally, see the in-plane velocity vectors in Fig. 10(c) and the surface friction lines in Fig. 15(a).

The surface skin friction lines presented in Fig. 15(a) provide a visual impression of the flow topology in the riblet case. The green lines depict the separation or reattachment lines. They present the locus of points on which the streamwise wall skin friction is zero. The length of the separation zone can be quantified as the streamwise distance between the separation line and the reattachment line. One can see that, in comparison to the baseline case, the length of the separation zone near the DL is shortened obviously, whereas the length near the CL shows no apparent variation [see Fig. 15(b) for a quantitative comparison]. The reversed flow region along the spanwise direction is also presented in Fig. 15(a), and one can clearly see that the area of the separation zone near the diverging region are significantly decreased, and near the converging region they are increased. In order to aid a quantitative comparison, the spanwise variations in the area of the separation zone per unit spanwise length (normalized by the separation area of the baseline case) is presented in Fig. 15(c). It can be seen that the area of the separation zone in the riblet case varies

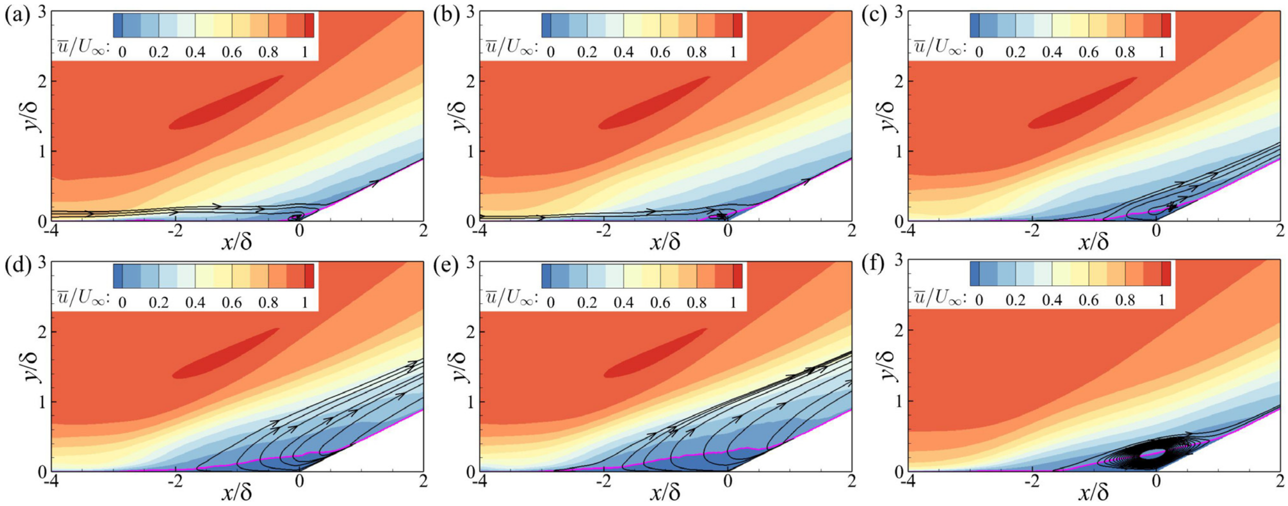

FIG. 14. Contours of the mean streamwise velocity in the *x-y* plane in the riblet case at (a) $z/\Lambda = 0.0$ (DL), (b) $z/\Lambda = 0.2$, (c) $z/\Lambda = 0.3$, (d) $z/\Lambda = 0.4$, (e) $z/\Lambda = 0.5$ (CL), and that (f) in the baseline case. The pink line depicts the locus of zero-streamwise-velocity with its starting and end points denoting the location of flow separation and reattachment.

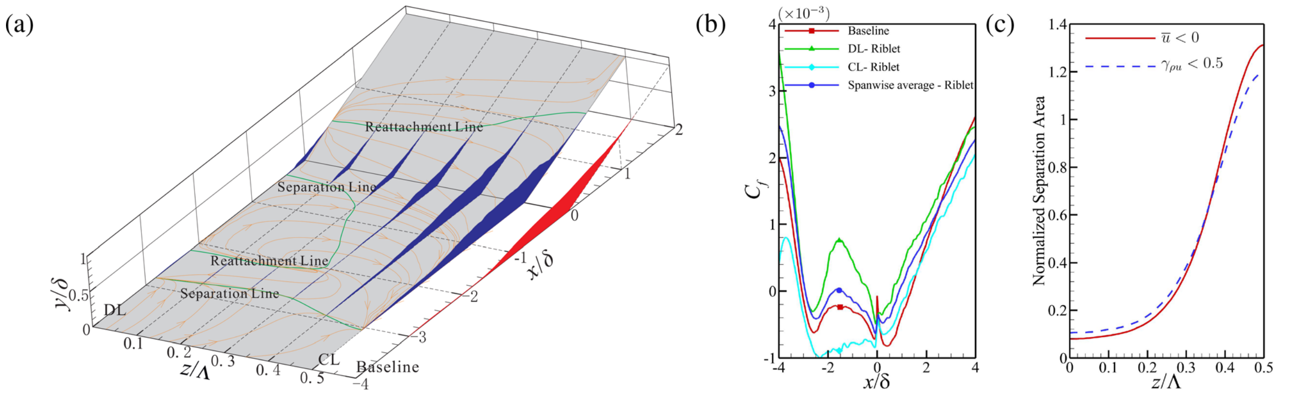

FIG. 15. (a) The separation region with the reversed flow ($\bar{u} < 0$) in the vicinity of the compression corner at several spanwise positions for the riblet case (blue color) and that for the baseline case (red color). The green lines depict the separation or reattachment lines; the orange lines denote the surface skin friction lines. (b) Streamwise distribution of the mean skin friction coefficient C_f in the vicinity of the compression ramp corner in the riblet case over the DL/CL and in the baseline case. (c) The spanwise variation in the area of the separation zone per unit span (normalized by the separation area of the baseline case) using the criterion of $\bar{u} < 0$ (the solid red line) and $\gamma_{\rho u} < 0.5$ (the dashed blue line).

significantly across the span. The spanwise portion around the DL experiences a dramatic reduction of 92% and the portion next to the CL reveals a considerable increase of 31%, resulting in a net reduction of 56% in the area of the spanwise-averaged separation zone.

Simpson[33] introduced a way of defining flow separation based on a statistical quantity, $\gamma_{\rho u}$, which denotes the fraction of the total time that the instantaneous flow moves downstream. According to the definition of Simpson,[33] incipient detachment (ID) occurs with instantaneous backflow 1% of the time, i.e., $\gamma_{\rho u} = 0.99$; intermittent transitory detachment (ITD) occurs with instantaneous backflow 20% of the time, i.e., $\gamma_{\rho u} = 0.8$; transitory detachment (TD) occurs with instantaneous backflow 50% of the time, i.e., $\gamma_{\rho u} = 0.5$. The streamwise location where $\gamma_{\rho u} < 0.5$ usually indicates the occurrence of the mean flow separation ($\bar{u} < 0$). The contours of $\gamma_{\rho u}$ in the *x-y* plane around the compression ramp in the riblet and baseline cases are presented in Fig. 16. The blue, green, and red lines denote the iso-lines of $\gamma_{\rho u} \equiv 0.99$, $\gamma_{\rho u} \equiv 0.8$, and $\gamma_{\rho u} \equiv 0.5$, respectively, representing the occurrence of ID, ITD, and TD. In comparison with the baseline case, the area with $\gamma_{\rho u} < 0.99$, $\gamma_{\rho u} < 0.8$, and $\gamma_{\rho u} < 0.5$ is decreased/increased over the DL/CL and tends to increase along the spanwise direction from the DL to the CL, consistent with the spanwise variation trend of the mean flow separation presented in Fig. 14. In addition, it is interesting to find that there exist two distinct separation zones (denoted by $\gamma_{\rho u} < 0.5$) around the diverging region, same with

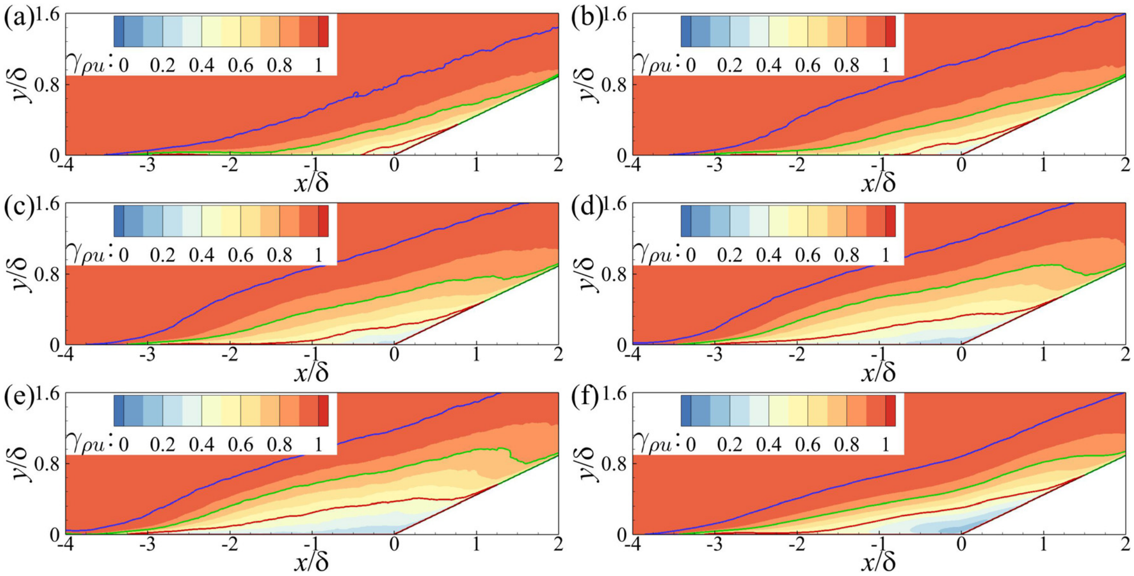

FIG. 16. Contours of $\gamma_{\rho u}$ in the *x-y* plane in the riblet case at (a) $z/\Lambda = 0.0$ (DL), (b) $z/\Lambda = 0.2$, (c) $z/\Lambda = 0.3$, (d) $z/\Lambda = 0.4$, (e) $z/\Lambda = 0.5$ (CL), and (f) that in the baseline case. The blue, green, and red lines denote the locus of $\gamma_{\rho u} \equiv 0.99$, $\gamma_{\rho u} \equiv 0.8$, and $\gamma_{\rho u} \equiv 0.5$, respectively.

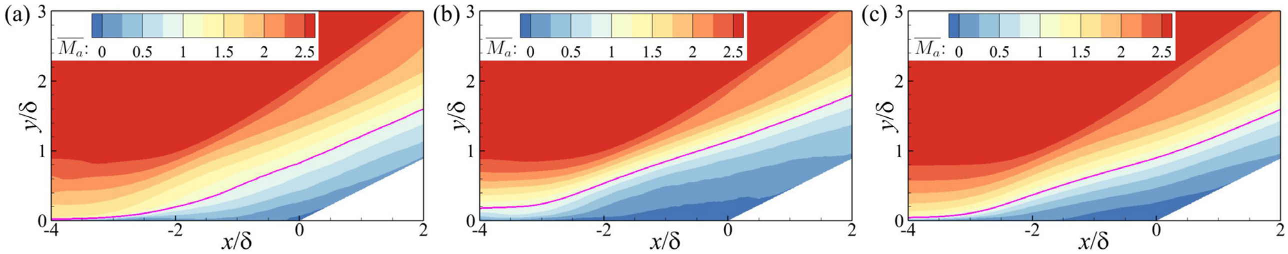

FIG. 17. Contours of the Mach number $\overline{M_a}$ in the x-y plane in the riblet case at (a) $z/\Lambda = 0.0$ (DL), (b) $z/\Lambda = 0.5$ (CL), and (c) that in the baseline case. The pink line depicts the iso-line of $\overline{M_a} \equiv 1$.

the mean flow separation shown in Fig. 14. This further confirms the occurrence of two separation regions around the DL. The similar phenomenon was also observed in a recent DNS study of an oblique shock-wave/flat-plate boundary layer interaction by Fang *et al.*[34] The spanwise variation in the area of $\gamma_{\rho u} < 0.5$ is presented in Fig. 15(c) (the dashed blue line). One can see that the distribution of the area of $\gamma_{\rho u} < 0.5$ exhibits a quite similar trend with that of the mean flow separation area defined by $\bar{u} < 0$, which indicates that using the criterion of $\gamma_{\rho u} < 0.5$ to define the flow separation is credible in flows over CD riblets.

It is not surprising to see that CD riblets are capable of mitigating the shock-induced flow separation around the diverging region, and the control mechanism can be attributed into two aspects: (1) the downwelling motion injects the high-momentum fluid with increased streamwise velocity and fluid density toward the wall; (2) the spanwise velocity transports the low-momentum fluid (low-streamwise velocity and low fluid density) away toward the converging region. In contrast, the area of the low-speed region around the CL increases and a much larger reverse flow region is observed, due to an increased intensity of the upwelling and a collection of the low-momentum fluid transported from the diverging region.

2. Mach number

Figure 17 presents contours of the mean local Mach number ($\overline{M_a}$) in the streamwise-vertical (x-y) plane in the riblet case over the DL/CL and the baseline case. As the flow approaches the compression corner, the region with low $\overline{M_a}$ is enlarged through the interaction region and the sonic line tends to move away from the wall, leading to a larger subsonic region. In comparison with the baseline case, the mean sonic line is closer to the wall upstream of the separation bubble, while the opposite trend is observed for the sonic line over the CL. This result is consistent with the trend of variations in the streamwise velocity shown in Fig. 14. In addition, the increased temperature around the converging region [see Fig. 12(c)] increases the speed of sound, and this further decreases the Mach number nearby. It is worthwhile mentioning here that the effectively decreased Mach number upstream of the separation shock around the converging region can lead to a reduced intensity of the separation shock (see Figs. 19 and 20) that helps ease the enlargement of the separation area nearby and alter the interaction region characteristics.[35] The same function of the upwelling has also been observed by Ali *et al.*[35] who conducted the experimental study by applying an array of high-momentum microjets upstream of a compression corner to control the shock-induced flow separation.

3. Pressure

The contours of the mean pressure on the x-y plane for the riblet case over the DL/CL and the baseline case are presented in Fig. 18. It can be seen that as the flow approaches the compression corner, the pressure rises significantly through a series of compression waves. The variation trend for each case behaves in a quite similar manner, especially in the region with $y/\delta > 1$. The main difference is that the near-wall pressure rising in the riblet case delays, owing to the decrease of the flow separation area. To examine the pressure distribution more closely, the contours of the magnitude of the pressure gradient $|\nabla \bar{p}|$ are presented in Fig. 19. It is clear that the magnitude of $|\nabla \bar{p}|$ at $y/\delta < 1$ over the converging region has an apparent reduction. This may result from the decrease of $\overline{M_a}$ and the increased region of $\overline{M_a} < 1$, both of which lead to a more gradual compression of the incoming flow relative to the separation shock of the baseline case.[35] To aid a quantitative comparison, the streamwise distribution of $|\nabla \bar{p}|$ at five vertical positions is plotted in Fig. 20. Compared with the

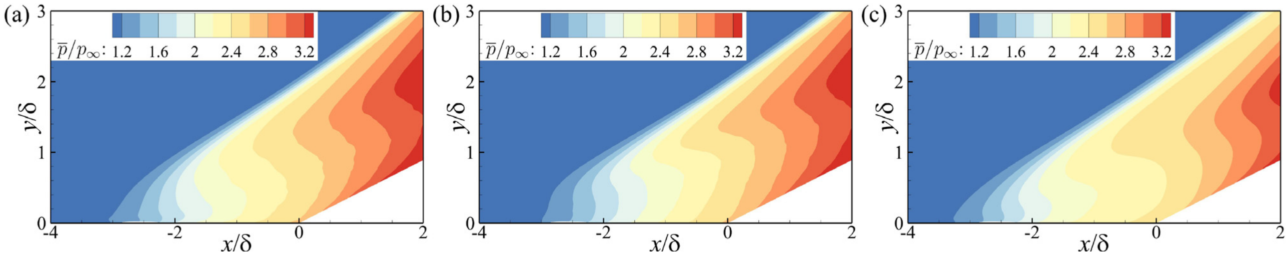

FIG. 18. Contours of the pressure in the x-y plane in the riblet case over the (a) DL and (b) CL as well as that (c) in the baseline case.

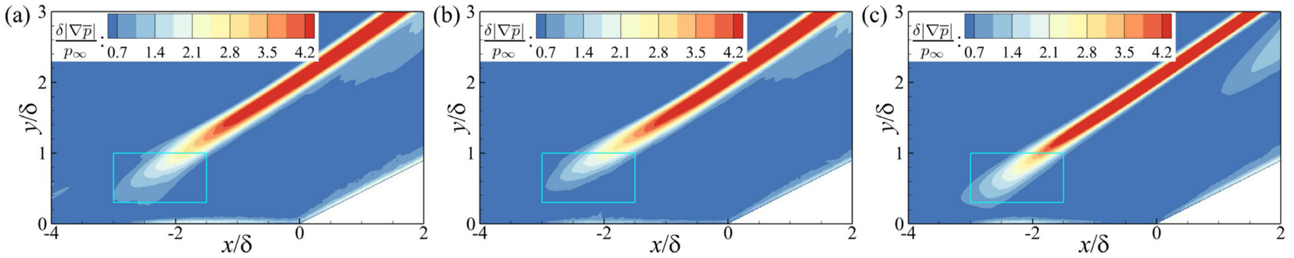

FIG. 19. Contours of the pressure gradient in the *x*-*y* plane in the riblet case over the (a) DL and (b) CL as well as that (c) in the baseline case. The cyan rectangular is located in the same position of (a), (b), and (c).

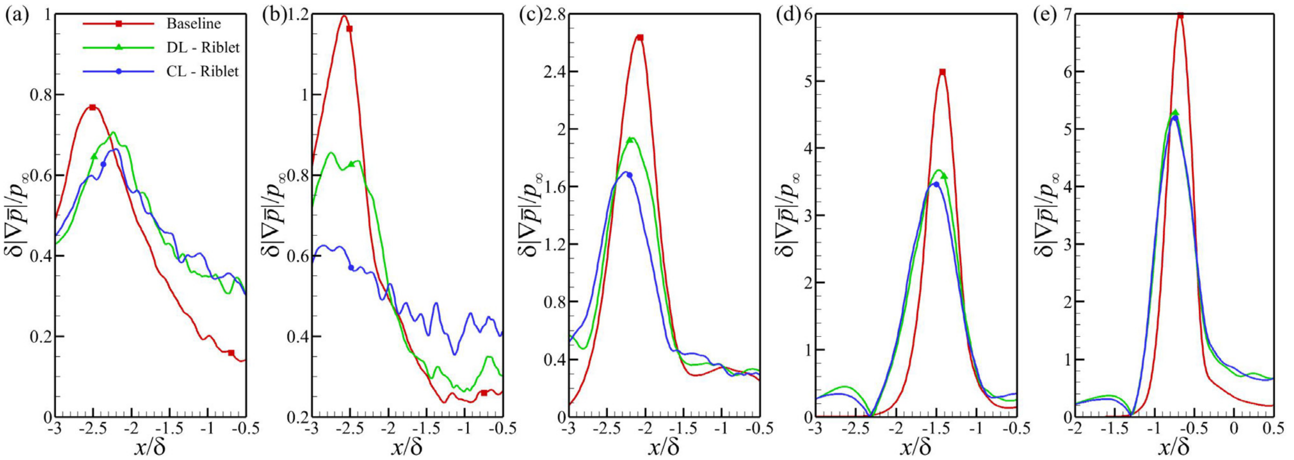

FIG. 20. Streamwise distribution of the pressure gradient for the riblet case over the DL/CL and that in the baseline case at (a) $y/\delta = 0$, (b) $y/\delta = 0.4$, (c) $y/\delta = 0.8$, (d) $y/\delta = 1.2$, and (e) $y/\delta = 1.6$.

baseline case, the pressure gradient for the riblet case has an apparent reduction, especially over the converging line. It is worthwhile mentioning that for the riblet case, no spanwise average is performed due to the spanwise heterogeneity and the resultant gradient terms (also the following second-order quantity) appear to be oscillating. Nevertheless, the variation trend can be clearly obtained.

In summary, CD riblets cause a reduction of the shock-induced separation area. This is because, on the one hand, the increased fluid momentum around the diverging region enhances the ability in mitigating the flow separation nearby. On the other hand, the upwelling motion caused by CD riblets around the converging line helps decrease the intensity of the separation shock[35] and, hence, eases the enlargement of the separation area due to the local lower energy fluid. Therefore, CD riblets appear to act as a boundary layer control method around the diverging region in some ways similar to what micro-vortex generators do[5] and behave like a shock control technique around the converging region.[35]

C. Impact of C–D riblets on the turbulent structures

1. Turbulence kinetic energy and Reynolds stress

The turbulence kinetic energy, $\langle k\rangle$, and the Reynolds shear stress, $\langle -u''v''\rangle$, in the flow over and downstream of the riblet section are presented in Figs. 21 and 22. In comparison with the baseline case, $\langle k\rangle$ and $\langle -u''v''\rangle$ at $x/\delta = -6$ and $x/\delta = -3$ for the riblet case appear to decrease slightly around the DL, while they exhibit an apparent increase around the CL with the peak moving away from the wall. Such an apparent spanwise heterogeneity is owing to the downwelling and upwelling associated with the large-scale secondary flow induced by CD riblets. A similar spanwise distribution has also been observed from the experimental results of the incompressible turbulent boundary layer flow developing over CD riblets.[15,18] As the flow approaches the compression corner, an opposite spanwise variation trend of $\langle k\rangle$ and $\langle -u''v''\rangle$ is observed in the near-wall region [see Figs. 21(e) and 22(e)]. This results from the different area (height) of the separation zone and the free shear layer along the spanwise direction that will be analyzed in the following.

Figures 23 and 24 present contours of $\langle k\rangle$ and $\langle -u''v''\rangle$ in the *x*-*y* plane in the riblet case over the DL/CL and that in the baseline case. As the flow approaches the compression corner, both $\langle k\rangle$ and $\langle -u''v''\rangle$ are amplified significantly through the interaction region, consistent with the DNS results of Wu and Martin.[27] There exists two local amplification zones of $\langle k\rangle$ and $\langle -u''v''\rangle$: one is located in the same position with the separation shock and the other is located in the same position with the separated shear layer that will be discussed below. In comparison with the baseline case, the intensity of both $\langle k\rangle$

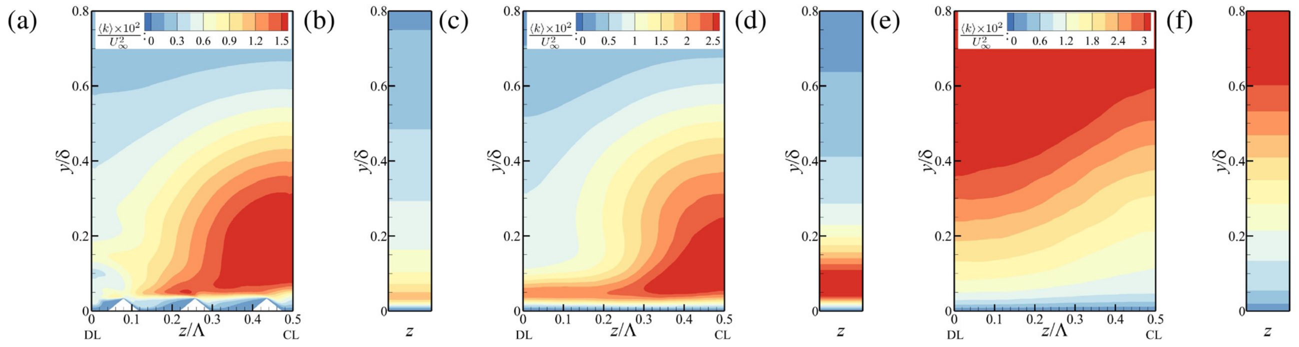

FIG. 21. Contours of the turbulence kinetic energy, $\langle k\rangle$, in the *y-z* plane at [(a) and (b)] $x/\delta = -6$, [(c) and (d)] $x/\delta = -3$, and [(e) and (f)] $x/\delta = 0$ for [(a), (c), and (e)] the riblet case and [(b), (d), and (f)] the baseline case.

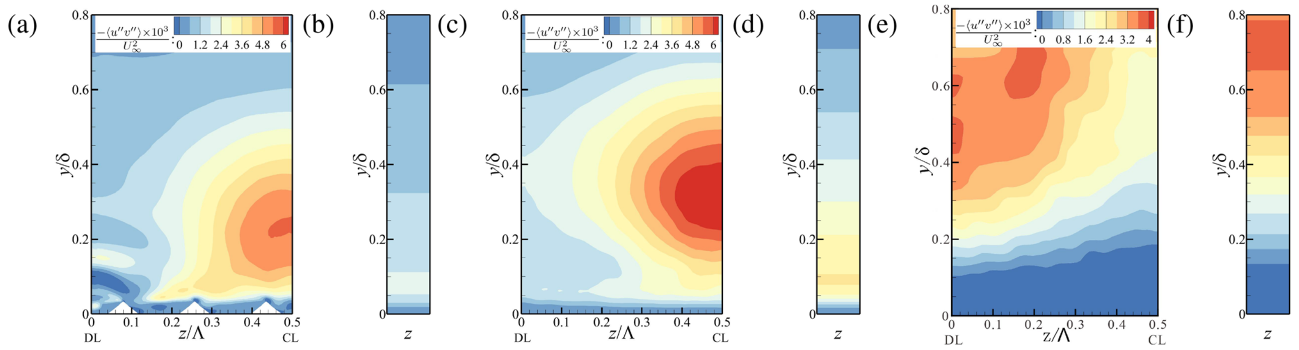

FIG. 22. Contours of the Reynolds shear stress, $\langle -u''v''\rangle$, in the *y-z* plane at [(a) and (b)] $x/\delta = -6$, [(c) and (d)] $x/\delta = -3$, and [(e) and (f)] $x/\delta = 0$ for [(a), (c), and (e)] the riblet case and [(b), (d), and (f)] the baseline case.

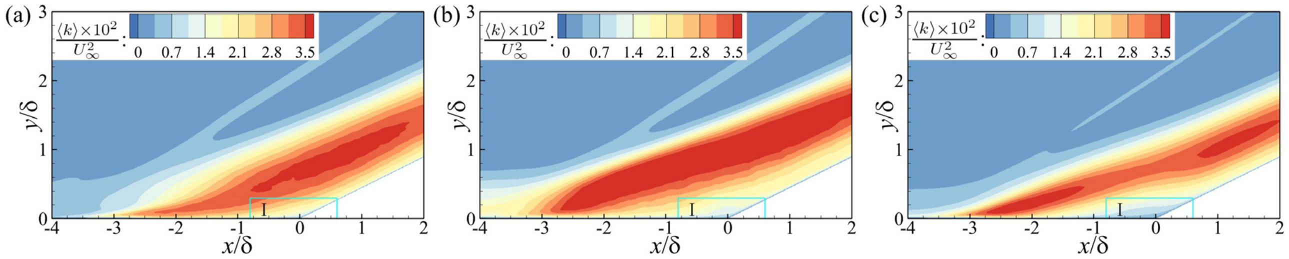

FIG. 23. Contours of the turbulence kinetic energy $\langle k\rangle$ in the *x-y* plane in the riblet case over the (a) DL and (b) CL as well as that (c) in the baseline case.

and $\langle -u''v''\rangle$ over the DL is decreased slightly, while they appear to increase significantly over the CL.

The separated shear layer denoted by the mean spanwise vorticity $\bar{\omega}_z = \frac{\partial \bar{v}}{\partial x} - \frac{\partial \bar{u}}{\partial y}$[34,36] is shown in Fig. 25. In comparison with the baseline case, the free shear layer in the *x-y* plane over the DL moves toward the wall with reduced intensity, owing to the decreased flow separation height. The opposite phenomenon occurs over the CL, resulting from the increased flow separation region. It is worth mentioning that the variation trend of $\bar{\omega}_z$ in the *x-y* plane over the DL/CL caused by CD riblets exhibits a similar pattern as that of $\langle k\rangle$ and $\langle -u''v''\rangle$. A strong correlation between them is not surprising. In fact, the turbulence amplification can be attributed to the generation of energetic turbulent structures in the free shear layer and the resultant shedding of these structures into the downstream.[36]

With a closer examination of $\langle k\rangle$ and $\langle -u''v''\rangle$ in the vicinity of the compression corner (Zone "I" in Figs. 23 and 24), it is found that $\langle k\rangle$ and $\langle -u''v''\rangle$ in the *x-y* plane over the DL are increased, owing to the moving-down of the free shear layer caused by the decreased flow separation height, and the opposite phenomenon occurs over the CL (Zone I in Fig. 25). This variation trend can also be seen in Figs. 21(e) and 22(e).

2. Instantaneous velocity field

To explore the influence of CD riblets on the near-wall turbulence structures, the instantaneous streamwise velocity in the wall-parallel

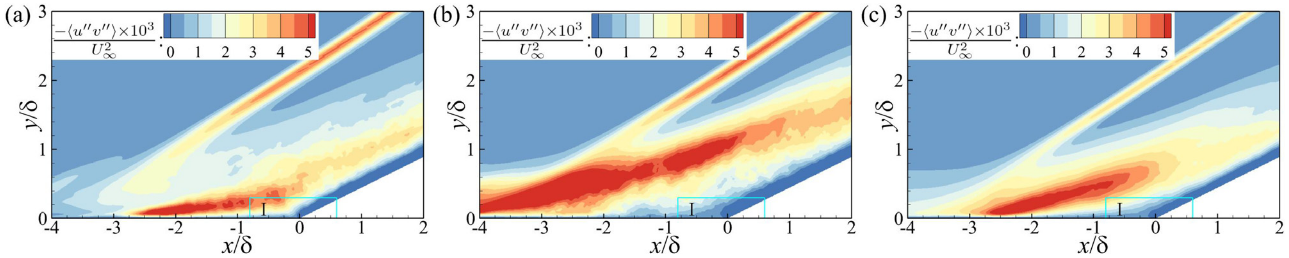

FIG. 24. Contours of the Reynolds shear stress $\langle -u''v''\rangle$ in the *x-y* plane in the riblet case over the (a) DL and (b) CL as well as that (c) in the baseline case.

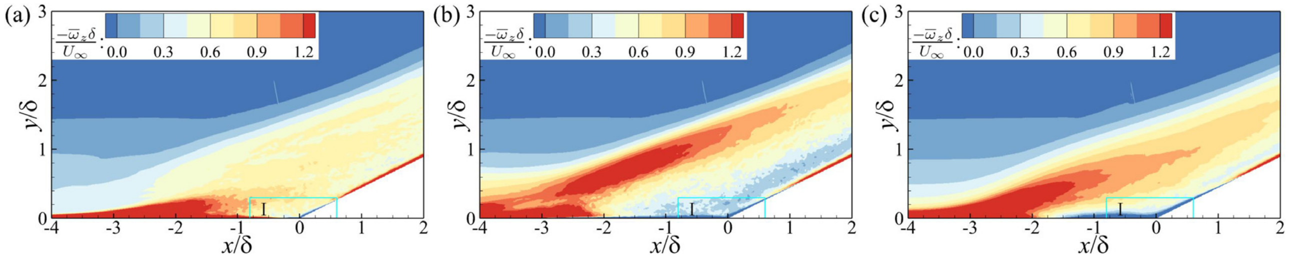

FIG. 25. Contours of the mean spanwise vorticity $\bar{\omega}_z$ in the *x-y* plane in the riblet case over the (a) DL and (b) CL as well as that (c) in the baseline case.

plane slightly above the riblet crest at a wall-normal distance of 0.05δ (15 wall units) is shown in Fig. 26. In the baseline case, the streamwise-aligned high/low-speed streaks occur randomly upstream of the separation region [Fig. 26(b)]. These meandering streaks are known as the velocity streaks in an equilibrium turbulent boundary layer, induced by the near-wall turbulence coherent structures which take the form of hairpin vortices and clusters of hairpin vortices.[37] The approximate spacing between the adjacent streaks in the baseline case is about 90–110 wall units which is close to the typical distance between adjacent low-speed streaks of $\Delta z^+ = 100$.[31] In the riblet case, the similar structures are observed upstream of the riblet section, while the near-wall flow over the riblet section is dominated by much wider high/low-speed streaks occurring over DL/CL. Apparently, these wide streaks result from the large-scale secondary flow, and the high/low-speed streaks are locked with the DL/CL, respectively. In the interaction region, the spanwise heterogeneity is still observed with decreased/increased low-speed area around the diverging/converging region, which is consistent with the spanwise variation trend of the mean streamwise velocity, as seen in Fig. 14. Note that for the riblet case, the actual vertical distance between the wall-parallel plane and the riblet tip is very small (only 0.017δ with five wall units), leading to a smaller streamwise velocity over the riblet section than that of the baseline case.

3. Instantaneous turbulence coherent structures

Q-criterion[38] has been widely used to visualize the turbulence coherent structures. The instantaneous iso-surfaces of $Q \equiv 0.5$, colored by the instantaneous streamwise vorticity, ω_x, in the riblet and

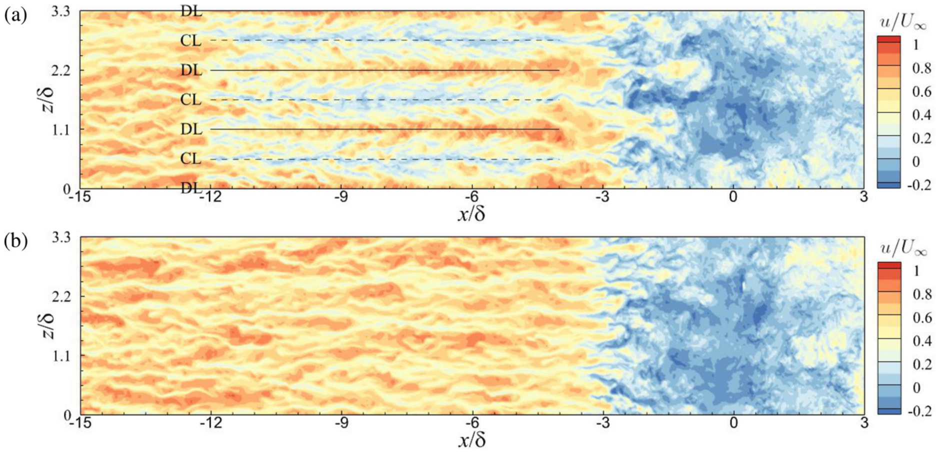

FIG. 26. Contours of the instantaneous streamwise velocity in the wall-parallel plane with $y = 0.05\delta$ (15 wall units) for (a) the riblet case and (b) the baseline case.

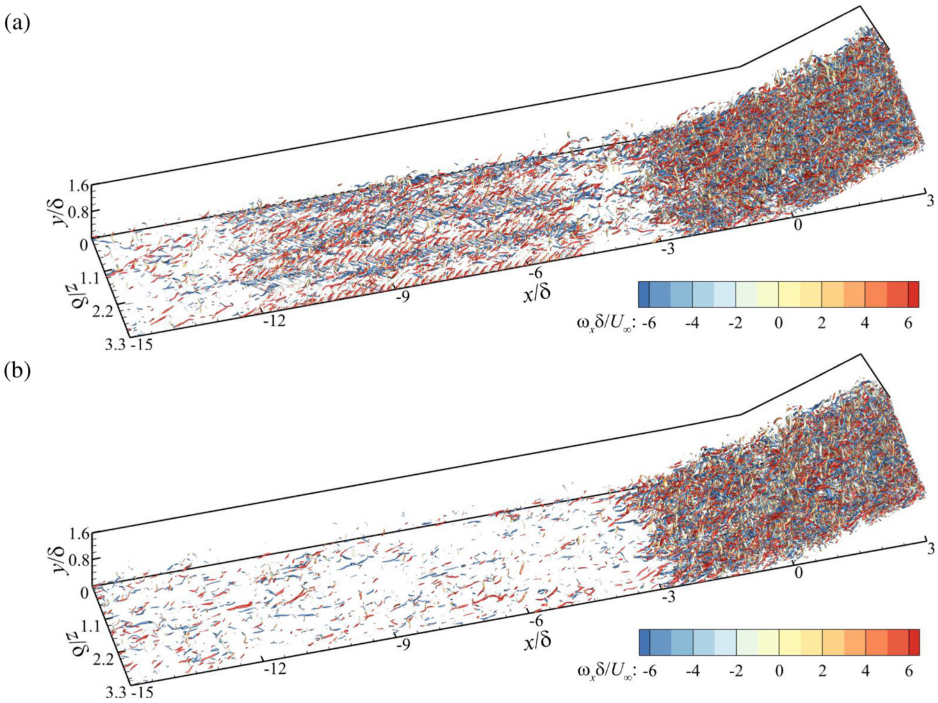

FIG. 27. Instantaneous turbulence coherent structures visualized using the iso-surfaces of $Q \equiv 0.5$ for (a) the riblet case and (b) the baseline case in the near-wall region ranging from $x/\delta = -15$ to $x/\delta = 3$. The iso-surfaces are colored by instantaneous streamwise vorticity ω_x.

baseline cases, are shown in Fig. 27. Upstream of the separation region, classic hairpin vortices and streamwise vortices with positive and negative vorticity appear to distribute randomly in the baseline case, while for the riblet case, an increased number of vortical structures are observed over the riblet section, indicating that the turbulent activities are amplified by the CD riblets. Furthermore, the vortices seem to accumulate themselves close to the converging region, and the number of vortices is relatively sparse near the diverging region. This finding is consistent with the DNS study preformed by Benschop and Breugem[19] and the experimental study conducted by Xu *et al.*[16] in the incompressible flow. The evidence here supports the hypothesis that the up-welling motion induced by the secondary flow motion is responsible for the enhancement of local turbulence. Similar observations have been previously reported in the incompressible flows.[39,40] As the flow approaches the interaction zone, the turbulence coherent structures are significantly increased for both the riblet and the baseline cases, resulting from the detachment of the flow and the subsequent separated shear layer.[34] The enhanced visualization of turbulence coherent structures in the vicinity of the interaction zone is shown in Fig. 28 using the iso-surface of $Q \equiv 1$. For the riblet case, there is still a spanwise heterogeneity with increased intensity occurring around the converging region, while the turbulence structures for the baseline case seem randomly distributed across the spanwise direction and the intensity tends to increase along the streamwise direction from $x/\delta = -3$ where the mean flow separation occurs (Fig. 14).

IV. CONCLUSION

In this paper, the effect of CD riblets on the separated flow over a compression ramp in a Mach 2.9 turbulent boundary layer is investigated using direct numerical simulation (DNS) at $Re_\theta = 2240$. The influence of CD riblets on the flow field upstream of and around the SWBLI zone is examined, and the control mechanism in mitigating the shock-induced flow separation has been obtained.

It is established from this study that, despite their small riblet height ($h = \delta/30$ and $h^+ = 10.2$), CD riblets are capable of producing a large-scale secondary flow in the wall-normal-spanwise plane with

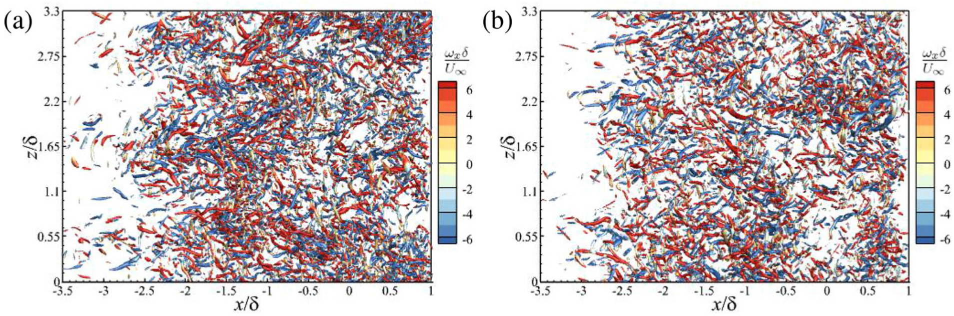

FIG. 28. Instantaneous turbulence coherent structures in the top view using the iso-surfaces of $Q \equiv 1$ in the vicinity of the interaction zone for (a) the riblet case and (b) the baseline case ranging from $x/\delta = -3$ to $x/\delta = 1$. The iso-surfaces are colored by instantaneous streamwise vorticity ω_x.

the downwelling obtained around the diverging region and upwelling near the converging region. This consequently leads to an apparent spanwise variation of the streamwise velocity, density, temperature, as well as the turbulent fluctuations and structures over the riblet section and in the interaction zone.

In comparison with the baseline case, the area of the separation zone experiences a dramatic reduction of 92% in the diverging region, owing to the downwelling that injects the high-momentum fluid toward the wall and the spanwise velocity that transport the low-momentum fluid away toward the converging region. The enhanced upwelling caused by CD riblets around the converging region, on the one hand, contributes to the decrease of the near-wall momentum and subsequently the increase of the local separation area. On the other hand, the upwelling can effectively reduce the incoming Mach number upstream of the compression corner. This appears to reduce the strength of the separation shock, leading to a more gradual compression of the incoming flow that helps ease the enlargement of the separation area nearby. Overall, the area of the separation zone reveals an increase of 31% around the converging region, and a net reduction of 56% in the spanwise-averaged separation area is achieved. To summary, CD riblets appear to act as a boundary layer control technique around the diverging region and behave like a shock control technique around the converging region.

The effect of CD riblets on the unsteady characteristics of the shock is outside the scope of this study and will be attempted in the future.

ACKNOWLEDGMENTS

This work was supported by the National Key Research and Development Program of China (No. 2019YFA0405300), NSFC Project (Nos. 91852203 and 12072349), and the Innovation Fund of Shanghai Aerospace Science and Technology (No. SAST2021-001). J. Fang acknowledges the UK Engineering and Physical Sciences Research Council (EPSRC) through the Computational Science Centre for Research Communities (CoSeC) and the UK Turbulence Consortium (No. EP/R029326/1).

AUTHOR DECLARATIONS

Conflict of Interest

The authors have no conflicts to disclose.

Author Contributions

Tongbiao Guo: Conceptualization (lead), Data curation (lead), Formal analysis (lead), Methodology (equal), Validation (equal), and Writing – original draft (lead). **Jian Fang:** Data curation (equal), Methodology (equal), Validation (equal), and Writing – review and editing (equal). **Ji Zhang:** Data curation (equal), Validation (equal), Writing – original draft (equal), and Writing – review and editing (equal). **Xinliang Li:** Data curation (equal), Methodology (equal), Software (equal), Validation (equal), and Writing – review and editing (equal).

DATA AVAILABILITY

The data that support the findings of this study are available from the corresponding author upon reasonable request.

APPENDIX: GRID-INDEPENDENCE STUDY

To ensure that the mesh resolution is sufficient for the field analysis, a grid-independence study is performed in the riblet case. DNS of four cases denoted by Case I, Case II, Case III, and Case IV is conducted with their mesh topology shown in Fig. 2, whereas for the four cases, the mesh is plotted every 10th/20th/30th/40th grid line in the streamwise direction. In the spanwise direction, the mesh distribution can be seen in Fig. 3(a), and for the four cases, the mesh is revealed every second/fourth/sixth/eighth grid line. The grid size in the wall-normal direction is same for all the cases since

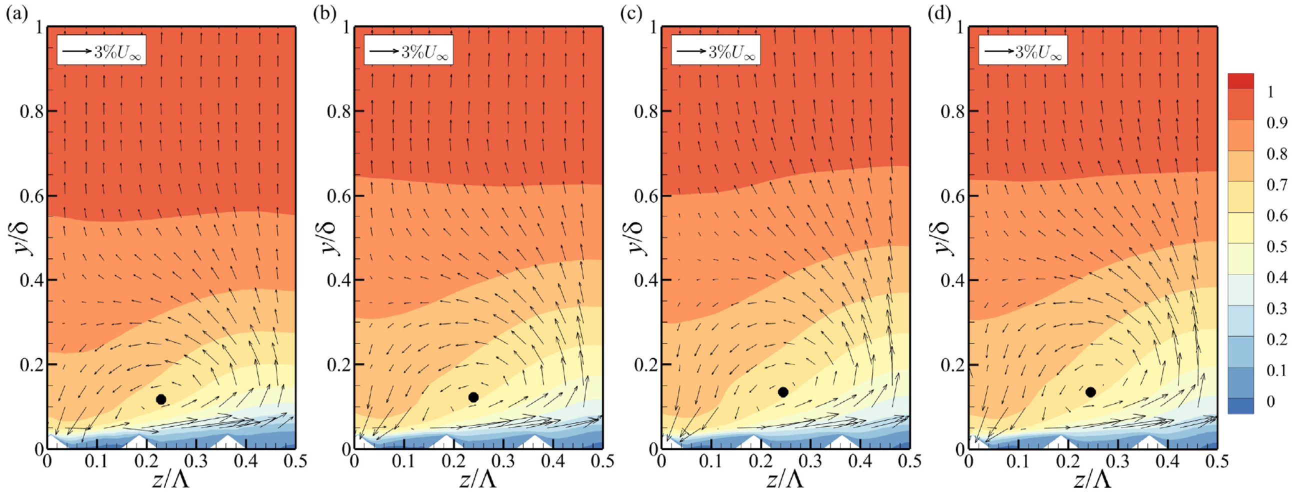

FIG. 29. Contours of the mean streamwise velocity superimposed with the in-plane velocity vectors in the y-z plane at $x/\delta = -6$ for (a) Case I, (b) Case II, (c) Case III, and (d) Case IV. The solid dot symbol indicates the center of the roll mode.

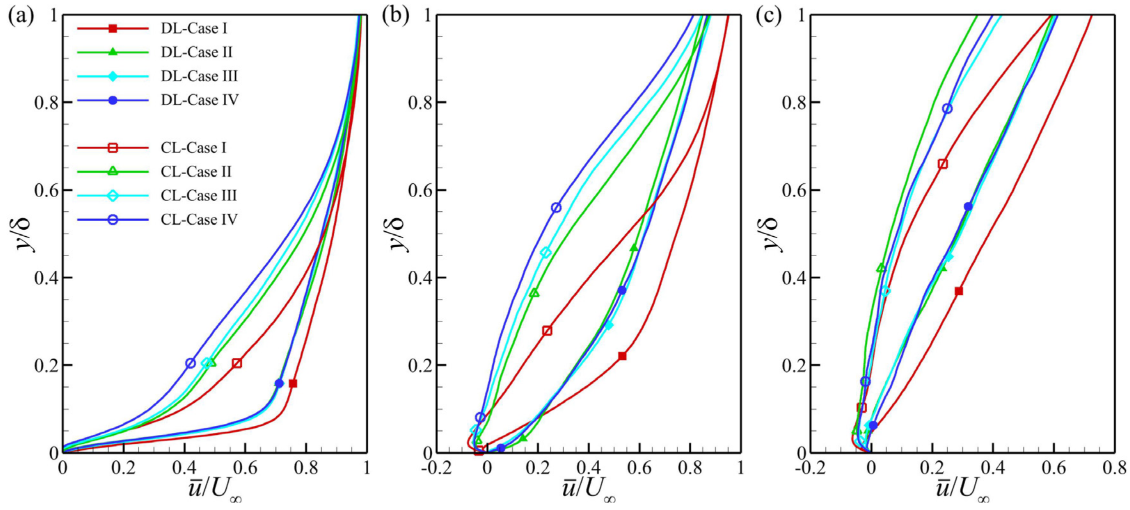

FIG. 30. Profiles of the mean streamwise velocity $\bar{u}$ at (a) $x/\delta = -3$, (b) $x/\delta = -1.5$, and (c) $x/\delta = 0$ over the DL and CL with different mesh densities.

it has been fine enough to resolve the wall turbulence in a DNS with the first grid point away from the wall satisfying $y^+ \leq 1$ as proposed by Sagaut.[41] In the present study, to ensure the resolution of the flow structures near the riblets, we further increase the mesh resolution by reducing the distance to the first point to $y^+ = 0.25$–0.45.

The contours of the mean streamwise velocity with the in-plane velocity vectors in the $y - z$ plane are displayed in Fig. 29 for the riblet case with different mesh densities. In comparison, there exists an apparent difference of the streamwise velocity distribution between Case I and Case II. As the mesh resolution increases, the results tend to converge, and no distinguishable differences can be seen in the streamwise velocity distribution and the roll mode center between Case III and Case IV.

Figure 30 shows profiles of the mean streamwise velocity $\bar{u}$ at $x/\delta = -3$, $x/\delta = -1.5$, and $x/\delta = 0$ over the DL and CL for all cases. One can see that as the mesh resolution increases, the profiles tend to converge, and the results for Case III and Case IV are very close to each other with the maximum error of around 2.5% U_∞ occurring at $x/\delta = 0$.

Figure 31 exhibits the streamwise distribution of the mean skin friction coefficient C_f and the mean wall pressure $\bar{p}_w$ in the vicinity of the compression ramp. As the mesh resolution increases, both C_f and $\bar{p}_w$ tend to converge, and the results between Case III and Case IV match quite well. Therefore, Case IV is expected to give sufficient resolutions and is used for the flow analysis in this paper.

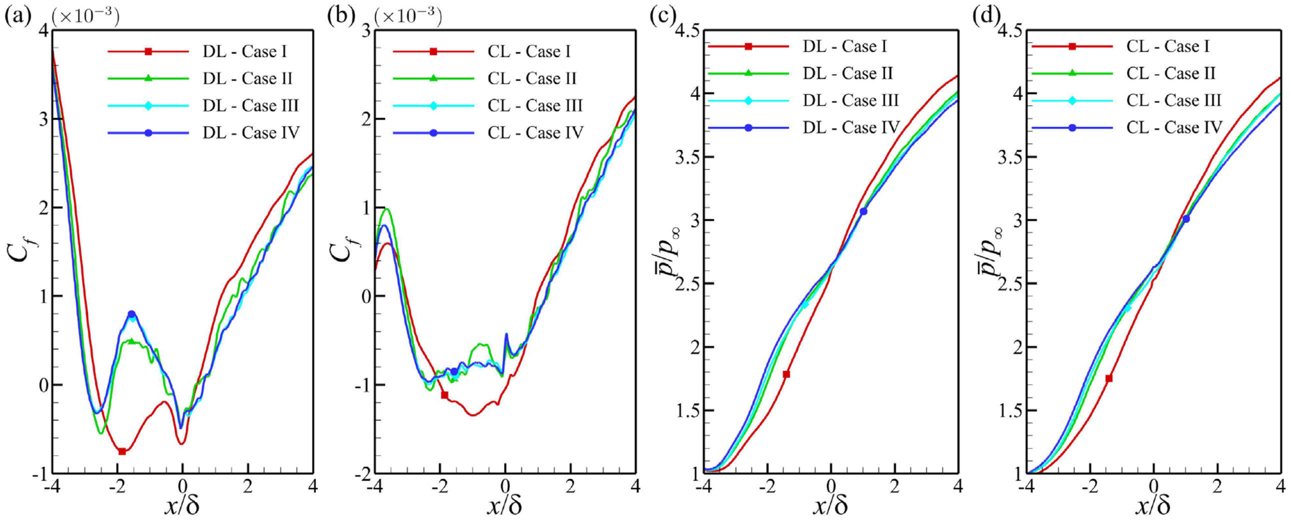

FIG. 31. Profiles of the [(a) and (b)] mean skin friction coefficient C_f and [(c) and (d)] the mean wall pressure $\bar{p}_w$ in the vicinity of the compression ramp over [(a) and (c)] the DL and [(b) and (d)] the CL.

REFERENCES

[1] R. Szwaba, "Comparison of the influence of different air-jet vortex generators on the separation region," Aerosp. Sci. Technol. **15**, 45–52 (2011).

[2] L. Feng, H. Wang, Z. Chen, Y. Zhou, and Y. Yang, "Unsteadiness characterization of shock wave/turbulent boundary layer interaction controlled by high-frequency arc plasma energy deposition," Phys. Fluids **33**, 015114 (2021).

[3] Y. Zhang, H. Tan, S. Sun, and C. Rao, "Control of cowl shock/boundary-layer interaction in hypersonic inlets by bump," AIAA J. **53**, 3492–3496 (2015).

[4] F. K. Lu, Q. Li, and C. Liu, "Microvortex generators in high-speed flow," Prog. Aerosp. Sci. **53**, 30–45 (2012).

[5] A. G. Panaras and F. K. Lu, "Micro-vortex generators for shock wave/boundary layer interactions," Prog. Aerosp. Sci. **74**, 16–47 (2015).

[6] D. Sun, Q. Guo, C. Li, and P. Liu, "Direct numerical simulation of effects of a micro-ramp on a hypersonic shock wave/boundary layer interaction," Phys. Fluids **31**(12), 126101 (2019).

[7] M. L. Funderburk and V. Narayanaswamy, "Experimental investigation of microramp control of an axisymmetric shock/boundary-layer interaction," AIAA J. **57**, 3379–3394 (2019).

[8] M. Rybalko, E. Loth, R. Chima, S. Hirt, and J. Debonis, "Micro-ramps for external compression low-boom inlets," AIAA Paper No. 2009-4206, 2009.

[9] K. Koeltzsch, A. Dinkelacker, and R. Grundmann, "Flow over convergent and divergent wall riblets," Exp. Fluids **33**, 346–350 (2002).

[10] H. Chen, F. Rao, X. Shang, D. Zhang, and I. Hagiwara, "Flow over bio-inspired 3D herringbone wall riblets," Exp. Fluids **55**, 1698 (2014).

[11] P. Quan, S. Zhong, Q. Liu, and L. Li, "Attenuation of flow separation using herringbone riblets at $M_\infty = 5$," AIAA J. **57**, 142–152 (2019).

[12] Q. Liu, S. Zhong, and L. Li, "Effects of bio-inspired micro-scale surface patterns on the profile losses in a linear cascade," J. Turbomach. **141**, 121006 (2019).

[13] T. Guo, S. Zhong, and T. Craft, "Control of laminar flow separation over a backward-facing rounded ramp with C-D riblets—The effects of riblet height, spacing and yaw angle," Int. J. Heat Fluid Flow **85**, 108629 (2020).

[14] B. Nugroho, N. Hutchins, and J. Monty, "Large-scale spanwise periodicity in a turbulent boundary layer induced by highly ordered and directional surface roughness," Int. J. Heat Fluid Flow **41**, 90–102 (2013).

[15] K. Kevin, J. P. Monty, H. Bai, G. Pathikonda, B. Nugroho, J. M. Barros, K. T. Christensen, and N. Hutchins, "Cross-stream stereoscopic particle image velocimetry of a modified turbulent boundary layer over directional surface pattern," J. Fluid Mech. **813**, 412–435 (2017).

[16] F. Xu, S. Zhong, and S. Zhang, "Statistical analysis of vortical structures in turbulent boundary layer over directional grooved surface pattern with spanwise heterogeneity," Phys. Fluids **31**, 085110 (2019).

[17] T. Guo, J. Fang, S. Zhong, and C. Moulinec, "Energy-based drag decomposition analyses for a turbulent channel flow developing over convergent–divergent riblets," Phys. Fluids **34**, 025115 (2022).

[18] F. Xu, S. Zhong, and S. Zhang, "Experimental study on secondary flow in turbulent boundary layer over spanwise heterogeneous microgrooves," Phys. Fluids **32**(3), 035109 (2020).

[19] H. Benschop and W.-P. Breugem, "Drag reduction by herringbone riblet texture in direct numerical simulations of turbulent channel flow," J. Turbul. **18**, 717 (2017).

[20] T. Guo, S. Zhong, and T. Craft, "Secondary flow in a laminar boundary layer developing over convergent-divergent riblets," Int. J. Heat Fluid Flow **84**, 108598 (2020).

[21] J. Duan, X. Li, X. Li, and H. Liu, "Direct numerical simulation of a supersonic turbulent boundary layer over a compression–decompression corner," Phys. Fluids **33**, 065111 (2021).

[22] F. Tong, D. Sun, and X. Li, "Direct numerical simulation of impinging shock wave and turbulent boundary layer interaction over a wavy-wall," Chin. J. Aeronaut. **34**, 350–363 (2021).

[23] F. Tong, X. Yuan, J. Lai, J. Duan, D. Sun, and S. Dong, "Wall heat flux in a supersonic shock wave/turbulent boundary layer interaction," Phys. Fluids **34**, 065104 (2022).

[24] Z. Zhang, F. Tong, J. Duan, and X. Li, "Direct numerical simulation of supersonic turbulent expansion corner with shock impingement," Phys. Fluids **33**, 105104 (2021).

[25] A. Jameson, W. Schmidt, and E. Turkel, "Numerical solution of the Euler equations by finite volume methods using Runge Kutta time stepping schemes," AIAA Paper No. 1981-1259, 1981.

[26] P. Bookey, C. Wyckham, A. Smits, and P. Martin, "New experimental data of STBLI at DNS/LES accessible Reynolds numbers," AIAA Paper No. 2005-309, 2005.

[27] M. Wu and M. P. Martin, "Direct numerical simulation of supersonic turbulent boundary layer over a compression ramp," AIAA J. **45**, 879–889 (2007).

[28] S. Pirozzoli, F. Grasso, and T. B. Gatski, "Direct numerical simulation and analysis of a spatially evolving supersonic turbulent boundary layer at M = 2.25," Phys. Fluids **16**, 530–545 (2004).

[29] X. Wu and P. Moin, "Direct numerical simulation of turbulence in a nominally zero-pressure-gradient flat-plate boundary layer," J. Fluid Mech. **630**, 5–41 (2009).

[30] P. R. Spalart, "Direct simulation of a turbulent boundary layer up to $R_\theta = 1410$," J. Fluid Mech. **187**, 61–98 (1988).

[31] J. Kim, P. Moin, and R. Moser, "Turbulence statistics in fully developed channel flow at low Reynolds number," J. Fluid Mech. **177**, 133 (1987).

[32] F. Xu, S. Zhong, and S. Zhang, "Vortical structures and development of laminar flow over convergent-divergent riblets," Phys. Fluids **30**, 051901 (2018).

[33] R. L. Simpson, "Turbulent boundary-layer separation," Annu. Rev. Fluid Mech. **21**, 205–232 (1989).

[34] J. Fang, A. A. Zheltovodov, Y. Yao, C. Moulinec, and D. R. Emerson, "On the turbulence amplification in shock-wave/turbulent boundary layer interaction," J. Fluid Mech. **897**, A32 (2020).

[35] M. Y. Ali, F. S. Alvi, R. Kumar, C. Manisankar, S. B. Verma, and L. Venkatakrishnan, "Studies on the influence of steady microactuators on shock-wave/boundary-layer interaction," AIAA J. **51**, 2753–2762 (2013).

[36] S. Priebe and M. P. Martín, "Low-frequency unsteadiness in shock wave–turbulent boundary layer interaction," J. Fluid Mech. **699**, 1–49 (2012).

[37] P. Moin and J. Kim, "Numerical investigation of turbulent channel flow," J. Fluid Mech. **118**, 341–377 (1982).

[38] J. Jeong and F. Hussain, "On the identification of a vortex," J. Fluid Mech. **285**, 69–94 (1995).

[39] W. Ni, L. Lu, J. Fang, C. Moulinec, D. R. Emerson, and Y. Yao, "Flow separation control over a rounded ramp with spanwise alternating wall actuation," Phys. Fluids **31**, 015101 (2019).

[40] C. Vanderwel, A. Stroh, J. Kriegseis, B. Frohnapfel, and B. Ganapathisubramani, "The instantaneous structure of secondary flows in turbulent boundary layers," J. Fluid Mech. **862**, 845–870 (2019).

[41] P. Sagaut, "Theoretical background: Large-eddy simulation," in *Large-Eddy Simulation for Acoustics*, Cambridge Aerospace Series, edited by C. Wagner, T. Hüttl, and P. Sagaut (Cambridge University Press, 2007), pp. 89–127.